

Mn(II)-based allysine-targeted molecular MR probes for imaging pulmonary fibrogenesis

Hua Ma¹, Iris Y. Zhou¹, Matthew Drummond², Nicholas Rotile¹, Rachel Knipe², Huan Wang¹, Eman Akam¹, Peter Caravan¹

¹Athinoula A. Martinos Center for Biomedical Imaging, Institute for Innovation in Imaging (i3), Department of Radiology, Massachusetts General Hospital, Harvard Medical School, Boston, USA, ²Division of Pulmonary and Critical Care Medicine and the Center for Immunology and Inflammatory Diseases, Massachusetts General Hospital, Boston, MA, USA.

Introduction: Idiopathic pulmonary fibrosis (IPF) is the most common and most severe type of interstitial lung disease, with unknown cause and a median survival of only 3 years. The presence of oxidized collagen, wherein lysine residues are converted to the aldehyde allysine, is a universal feature of fibrogenesis. Molecular MR imaging of fibrogenesis has the potential for early diagnosis of IPF and to monitor disease progression and treatment response. In this work, novel reversible allysine-targeting Mn(II)-based probes were synthesized that differed in their association and dissociation kinetics. The in-vivo efficiency for targeting lung fibrogenesis were tested in a bleomycin-induced mouse model.

Methods: Synthesis: The novel Mn-PC2A derivatives (Figure 1A) were synthesized in 6 steps from the pyclen macrocycle. **In vitro reaction kinetics and relaxivity measurement:**

Condensation kinetics of MnL1 and MnL3 with butyraldehyde and hydrolysis rate constant of the reaction product hydrazone were measured by UV spectroscopy and HPLC, respectively (25 °C, pH 7.4, PBS). MnL1, MnL3 and MnL4 were incubated with BSA (17.3 mg/mL) or allysine-modified BSA (BSA-Ald, 17.4 mg/mL, 260 μM aldehyde) at 37 °C for 3 h, and 1/T₁ was measured at 1.4 T, 37 °C, and plotted vs Mn concentration to obtain relaxivity. Protein bound MnL1 and MnL3 were isolated by ultrafiltration and relaxivity was measured. All Mn concentrations were measured by ICP-MS. **In vivo MRI:** C57Bl/6 male mice at 10-12 weeks of age received a single intratracheal dose of bleomycin (Bleo).¹ MRI was carried out 14 days after Bleo-injury. Age-matched Naïve mice were used as healthy control. Animals were imaged on a 4.7 T Bruker Biospec with following sequences and parameters: 3D Ultrashort TE (3D-UTE, TR/TE/FA=4 ms/ 11.75 μs/ 16°, 0.6 mm isotropic spatial resolution) images were acquired prior to and dynamically post injection of 100 μmol/kg contrast agent; Rapid Acquisition with Relaxation Enhancement (RARE, TR/TE/FA=1.5 s/ 8 ms/ 180°, 0.3 mm isotropic spatial resolution) and contrast enhanced T1-weighted 3D Fast Low Angle Shot (FLASH, TR/TE/FA=10 ms/ 2.56 ms/ 30°, 0.6 mm isotropic spatial resolution) images were acquired to define regions of interest (ROIs) in the lung that excluded vessels and airways. A total of 6 lung ROIs were defined on axial UTE images to obtain signal intensity (SI); ROIs in the dorsal muscle in each slice were also defined as reference. We averaged the lung-to-muscle ratio (LMR) from the 6 slices to calculate changes in LMR (ΔLMR) at each time point.

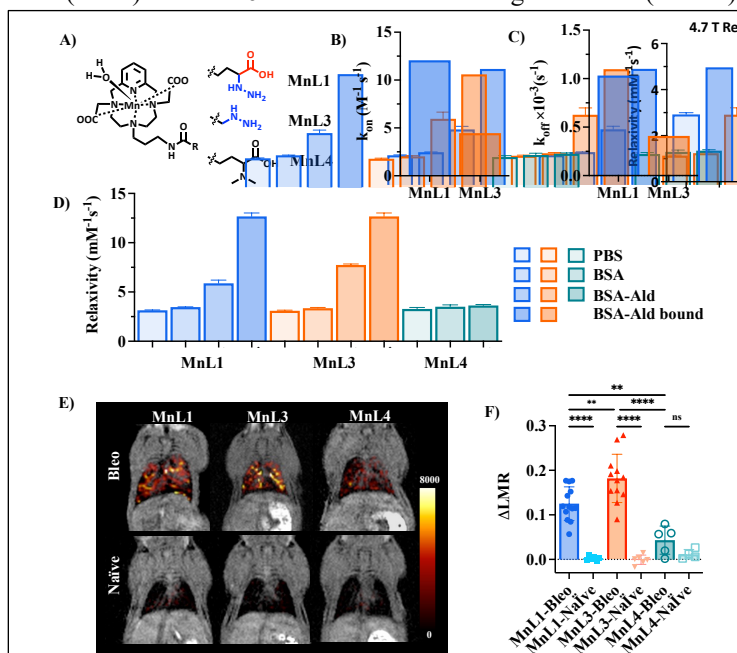


Figure 1. A) Structures of the probes. B) Condensation rate constants of MnL1 and MnL3 with butyraldehyde. C) Hydrolysis rate constants of hydrazone condensation product. D) Relaxivities of MnL1, MnL3 and MnL4 in PBS, in BSA solution, in allysine modified BSA-Ald, and bound to BSA-Ald. E) Coronal UTE MR images overlaid with false color image of lung enhancement generated by subtraction of pre- from 60 min post-injection UTE image. F) Quantification of the change in lung:muscle MR signal ratio in lungs of bleomycin-injured or naïve mice 60 min post-injection.

Results: The α-carboxylate moiety in MnL1 results in a 3-fold higher condensation rate constant compared to MnL3 (Figure 1 B). The hydrolysis rate constant of MnL1-hydrazone was 2-times higher than MnL3-hydrazone (Figure 1C). Relaxivities (Figure 1D) of MnL1 and MnL3 were similar in PBS (3 mM⁻¹s⁻¹), consistent with the presence of one coordinated water ligand. Relaxivities were not enhanced in BSA solution, but dramatically increased in the presence of BSA-Ald, which demonstrates specific binding to the latter and low/no nonspecific binding to the former. The relaxivities of the protein bound form of MnL1 and MnL3 were almost 4 times higher than the unbound form. The relaxivities of negative control probe (MnL4, which cannot react with aldehydes) were unchanged in BSA or BSA-Ald solution.

In bleomycin injured mice, both MnL1 and MnL3 showed significantly higher ΔLMR than in naïve mice and significantly higher ΔLMR than that of MnL4 in injected mice (Figure 1E, 1F). ΔLMR was also highly correlated with lung allysine measured ex vivo for MnL1 ($R^2 = 0.84$) and MnL3 ($R^2 = 0.87$). Overall, MnL3 was significantly superior to MnL1 at detecting fibrogenesis at all time points, e.g. ΔLMR at 60 min was 0.13 for MnL3 vs 0.18 for MnL1.

Conclusion: The novel hydrazine-bearing Mn(II) probes MnL1 and MnL3 enable specific binding to allysine, 4-fold turn on in relaxivity upon binding, and show potential for noninvasive imaging of lung fibrogenesis. Among these two candidates, MnL3 with greater hydrolytic stability (but slower on-rate) exhibited higher sensitivity in detecting fibrogenesis and highlights the significance of modulating bond dissociation kinetics in achieving higher probe sensitivity.

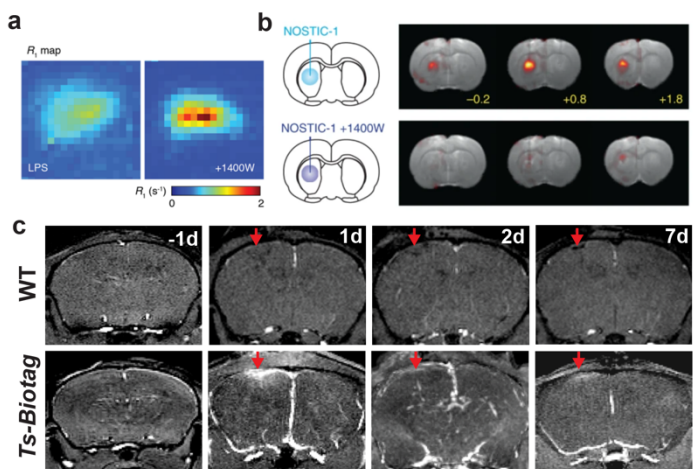
Reference: 1) Waghorn, Philip A., et al. Molecular Magnetic Resonance Imaging of Lung Fibrogenesis with an Oxyamine-Based Probe. Angew. Chem.-Int. Edit. 2017, 56: 9825-9828.

Molecular Tools to Resolve Neuroimmune Signaling with MRI:

Inflammatory signaling underlies nearly every incurable psychiatric and neurodegenerative disorder, but microglia, the predominant neuroimmune cells, remain one of least tractable types to study. Foundational methods of neuroscience and immunology such as multiphoton imaging, viral tools, flow cytometry and bone marrow transplants are all incompatible with the highly reactive and tissue bound microglia. Adequate tools to resolve and manipulate these cells *in vivo* would accelerate neuroimmune research from studies of basic biological function to disease mechanisms. My research takes a first principles approach to developing methods to sense neuroimmune signals with molecular specificity, express these tools in a humanized *in vivo* microglia model, and to image neuroimmune biology noninvasively over time.

This work is built around Molecular functional MRI (mfMRI) as the most suitable platform for noninvasive imaging with molecular specificity. We have demonstrated capabilities in detecting key neuroimmune molecules in several proof-of-concept experiments: **1)** Chemical and genetic MRI sensors of nitric oxide (NO) to resolve this key neuroimmune and neurovascular small molecule over time scales of seconds to days. **2)** An MRI signaling reporter for reactive oxidative species (ROS) for longitudinal imaging of neural injury and microglial responses to cancer. **3)** Label free inflammatory imaging with MR spectroscopy imaging (MRSI) with machine learning based analysis.

These approaches establish mfMRI as a viable tool for imaging neuroimmune molecules, characterizing microglial cell states, and profiling neuroinflammatory responses both longitudinally and noninvasively. Moreover, MRI offers a direct bridge from tractable model systems to human research.



Molecular sensor imaging of neuroimmune molecules with MRI. *R₁* map of an NO responsive reporter molecule in a living rat brain 24h post LPS administration (a) Infusion of iNOS inhibitor 1400W prevents NO release. Genetically controlled production of NO as a sensing modality using NOSTIC vs suppression with 1400W (b) Longitudinal imaging of control vs transgenic mice expressing the multimodal “Biotag” label under control of a ROS responsive “Ts” element (c).

Targeted Radiosensitizers for MR-Guided Radiation Therapy of Prostate Cancer

Dong Luo¹, Andrew Johnson², Matthew Bailey², Xinning Wang¹, Clemens Burda³, Thomas J. Meade², James P. Basilion¹

¹Department of Radiology, Case Western Reserve University, Cleveland, Ohio, United States, ²Department of Chemistry, Molecular Biosciences, Neurobiology, and Radiology, Northwestern University, Evanston, Illinois, United States, ³Department of Chemistry, Case Western Reserve University, Cleveland, Ohio, United States

Introduction: Although radiation therapy is highly effective for the majority of cancer patients, the nonspecificity of irradiation can result in toxicity for surrounding tissues, which is especially problematic for patients with tumor that require high radiation doses or are difficult to target. Magnetic resonance imaging (MRI) is a powerful clinical imaging modality that provides high-resolution three-dimensional images of soft tissues.¹ Magnetic resonance (MR) molecular imaging or molecular MRI of prostate cancer biomarkers, such as prostate-specific membrane antigen (PSMA), can facilitate non-invasive prostate cancer detection² and MRI-guided radiotherapy. The objective of this study is to develop a nanoparticle technology that will improve the success rate for prostate cancer diagnosis, precise cancer localization and radiation therapy.

Methods: **Synthesis:** Gd(III) complex and PSMA-targeted Au-Gd nanoparticles(NPs)/nanoclusters(NCs) were synthesized and characterized using published protocols.³ **In vitro uptake, MRI and radiotherapy:** Retrovirally transformed PSMA-positive PC3pip cells and transfection control PSMA-negative PC3flu cells were cultured and incubated with PSMA-targeted Au-Gd NPs/NCs to evaluate their selectivity and uptake, Au/Gd(III) per cell was measured by ICP. *In vitro* MR imaging of cells after 24 h of incubation was carried out using a Bruker Biospin 7 T magnet (Bruker Biospin, Billerica, MA, U.S.A.). Au-Gd NC uptake in cells was also imaged using a Leica HyVolution SP8 confocal microscope. Cells were also irradiated with X-ray (Cs-137 with energy of 0.6616 Mev) and colony formation assay was used to evaluate radiosensitization by Au-Gd NPs/NCs. **In vivo MRI and radiotherapy:** All animal experiments were performed in accordance with approved guidelines by the Case Western Reserve University IACUC committee. Nude mice with flank tumors, PC3pip tumor or PC3flu tumor, were used to evaluate the active targeting of Au-Gd NPs/NCs and MR imaging. Mice (n = 3) were injected (i.v.) with Au-Gd NPs/NCs at 60 μ mol Gd(III)/kg body weight. Mice were imaged by MR on a Bruker Biospin 7 T magnet before and 0.5 h, 1 h, 2 h, 3 h, 4 h, 6 h, 8 h and 24 h after injection using a spin echo sequence (TR = 500 ms, TE = 8.1 ms, flip angle = 180°, NEX = 3, FOV = 20×20 mm², slice thickness = 1 mm, and matrix size = 256×256). X-ray irradiation of tumor (6 Gy) was carried out at 4 h post-injection and DWI images were obtained for each animal's tumor using a DWI-EPI (echo planar imaging) acquisition (TR/TE = 2000 / 27 ms. b = 0 and 500 s/mm², FOV = 17.6×16 mm, matrix = 110×100 , slice thickness = 1mm, 3 signal averages, and 4 EPI segment / TR). All raw data was exported for offline analysis in Matlab and apparent Diffusion Coefficient (ADC) maps were obtained for each imaging slice. Radiotherapy outcome was also monitored by measuring the tumor growth over 30 days.

Results: PSMA-targeted Au-Gd NPs/NCs had an average hydrodynamic size of 7.8 nm and 8.3 nm, respectively. Conjugating Gd(III) complex to AuNPs significantly improved the r_1 relaxivity to $20.6 \text{ mM}^{-1} \text{ s}^{-1}$, compared to only $5.5 \text{ mM}^{-1} \text{ s}^{-1}$ for the free Gd(III) complex. For the Au-Gd NCs with Gd(III) conjugated directly to the PSMA-1 ligand, r_1 relaxivity was $7.5 \text{ mM}^{-1} \text{ s}^{-1}$. *In vitro* cellular uptake experiments demonstrated significantly higher Au-Gd NPs/NCs uptake in PC3pip cells than in PC3flu cells. Not surprisingly, the PC3pip cells demonstrated a greater (brighter) MR contrast at 7T than the PC3flu cells, and the signal-to-noise ratio increase for PC3pip cells was 4.2 times of that for PC3flu cells. After radiation, the Au-Gd NPs also enhanced radiotherapy for PC3pip cells and thus PC3pip cells were selectively killed. *In vivo*, MRI results demonstrated higher accumulation and MR contrast of targeted Au-Gd NPs in PC3pip tumors than in PC3flu tumors, with a contrast-to-noise ratio (CNR) of 13.9 and 5.64, respectively. X-ray irradiation of tumors resulted in increased ADC value and diminished PC3pip tumor.

Discussion: The use of PSMA-targeted Au-Gd NPs/NCs to differentiate between PSMA-positive and PSMA negative cells/tumors was tested here by monitoring the MR signals with the goal of using MR to guide radiation dose deposition. By conjugating the Gd(III) complex to the surface of nanoparticles, the r_1 relaxivity was significantly improved due to the surface effect and reduction of tumbling of Gd(III). The PSMA-1 ligand on NPs/NCs surface also enhanced recognition and uptake of the NP/NC by the PSMA positive PC3pip cells, achieving a higher intracellular Gd (III) and Au content for better MR contrast and radiosensitization. Au has excellent absorption of X-rays over soft tissue and the selective delivery of AuNPs/NCs can sensitize tissue to radiotherapy, increasing efficacy while decreasing the local radiation dose administered. This will potentially reduce the damage to healthy cells and tissue. This was evidenced by differential killing of PC3pip cells *in vitro* using mixed cell cultures of both PC3pip and PC3flu cells that had been treated with Au-Gd NPs.

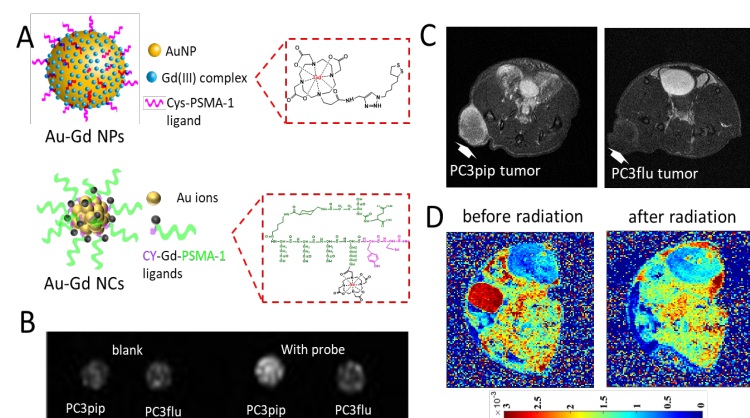


Figure 1. **A)** Schematic representation of PSMA-targeted Au-Gd NPs/NCs with Au as the core, Gd(III) complex as the stabilizer, and Cys-PSMA-1 as the targeting ligand. **B)** *In vitro* cell uptake and MR imaging, showing a higher uptake of Au-Gd NPs in PC3pip cells than in PC3flu cells and thus a greater MR contrast. **C)** *In vivo* T1-weighted spin echo images of mice with PC3pip tumor (left) and PC3flu tumor (right) showing tumor targeting of Au-Gd NPs. **D)** ADC maps of mice injected with Au-Gd NPs before and at 24 h after a single irradiation (6 Gy).

Conclusion: The nanoparticle system described herein is envisioned to provide early prostate cancer detection and permit MRI-guided precise radio-ablation of cancerous tissues with less damage to surrounding tissues. Three papers have resulted from this work: Luo et al., *Nano Lett* 2020; Luo et al., *Small*, 2019; and Luo et al., *Chemical Science*, 2019.

References: 1) Han Z, et al. Targeted gadofullerene for sensitive magnetic resonance imaging and risk-stratification of breast cancer. *Nature communications* 2017, 8, 692. 2) Banerjee, SR, et al. Synthesis and evaluation of Gd(III)-based magnetic resonance contrast agents for molecular imaging of prostate-specific membrane antigen. *Angewandte Chemie* 2015, 54, 10778-82. 3) Luo D, et al. Targeted Radiosensitizers for MR-Guided Radiation Therapy of Prostate Cancer. *Nano Lett.* 2020, 20, 7159-67.

Zinc Detection by MRI using a lanthanide complex-zinc finger peptide conjugate

Manon Isaac¹, Agnès Pallier², Laurent Barantin³, Frédéric Szeremeta², Olivier Sénèque¹, Célia Bonnet²

1. Université Grenoble Alpes, CNRS CEA, BIG, LCBM, Avenue des Martyrs, 38000 Grenoble, France

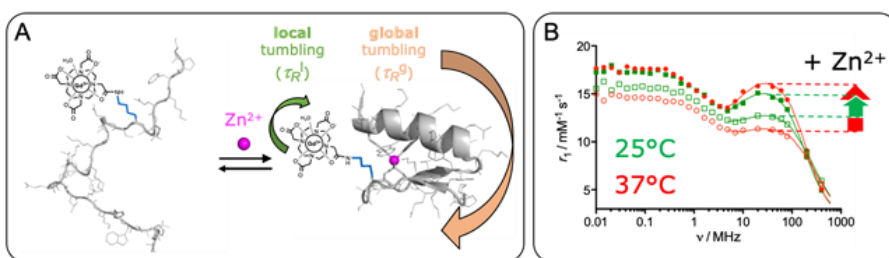
2. Centre de Biophysique Moléculaire, UPR 4301 CNRS, rue Charles Sadron, 45071 Orléans, France; celia.bonnet@cnrs-orleans.fr

3. Université de Tours, UMR1251, iBrain, Tours, France

Zinc is the second most abundant transition metal ion in humans, and it plays a central role in controlling gene transcription and metalloenzyme function. However, its quantitative distribution and its exact role are not well understood. It has also been shown that disturbances in Zn²⁺ homeostasis is implicated in neurodegenerative diseases (Alzheimer, Parkinson), diabetes, and cancers (prostate, pancreas and breast).¹ Therefore, monitoring Zn²⁺ *in vivo* by non-invasive technique such as MRI is important in biomedical research to understand its biological role, and to provide earlier diagnosis for specific pathologies. Zn²⁺ is not only an important biomarker but also a target adapted for MRI as it is present in the extracellular media, and the pool of labile Zn²⁺ is in the MRI detectable concentration range. For example, Zn²⁺ is in mM concentration scale in the prostate and pancreas and can be released upon glucose stimulation. In the blood the concentration is in the 10 μM range and reaches 300 μM in the brain.²

Zn²⁺-responsive Gd-based contrast agents (CAs) is a rapidly growing field pushed forward by the recent *in vivo* successes of Zn²⁺ detection in the pancreas or prostate.³ The Gd³⁺-based CA used so far are mainly small molecular systems using dipicolylamine, iminodiacetate, or quinoline units for Zn²⁺ complexation.⁴

Natural Zn-binding proteins are an interesting alternative to small molecules as selective metal-binding units. Zinc finger (ZF) proteins constitute a wide class of Zn-binding proteins and classical ββα ZF constitute one of the most important family of ZF, being encountered in many transcription factors.⁵ Peptides having this sequence have no defined conformation in their free (zinc-unbound) form and adopt a ββα fold when they bind Zn²⁺.⁶



We will present the design of zinc responsive CAs based on a ZF peptide, and show that the system displays a 40 % relaxivity increase at 37°C and 20 MHz upon Zn²⁺ binding, which is ascribed to the folding

of the peptide (Figure). This response is rationalized by determining the microscopic parameters of the system. We will also discuss the selectivity of the system, and show that the replacement of the Gd³⁺ ion by a Tb gives a luminescent probe.⁷

1. Dick, R. et al. *Am. J. Alzheimers Dis. Other Demen.* **2010**, *25*, 572 ; Kelleher, S.L. et al., *Adv. Nutr.*, **2011**, *2*, 101-111.
2. De Leon-Rodriguez et al., *Inorg. Chim. Acta* **2012**, *393*, 12-23
3. Lubag A.J.M. et al, *Proc. Natl. Acad. Sci. U. S. A.* **2011**, *108*, 18400–18405; Jordan M.V.C. et al., *Proc. Natl. Acad. Sci. U. S. A.* **2016**, *113*, E5464–E5471
4. Bonnet C.S. *Coord. Chem. Rev.* **2018**, *369*, 91.
5. Klug A., *Annu. Rev. Biochem.* **2010**, *79*, 213–231
6. Krizek B. et al., *J. Am. Chem. Soc.* **1991**, *113*, 4518–4523
7. Isaac, M. ; Pallier, A. et al, *Chem. Commun.* **2018**, *54*, 7350-7353.

Next-generation Clinical-scale Instrumentation for Parahydrogen-Induced Polarization

Shiraz Nantogma,¹ Isaiah Adelabu,¹ Nuwandi M. Ariasingha,¹ Anna Samoilenco,¹ Md Raduanul H. Chowdhury,¹ Mohammad S. H. Kabir,¹ Boyd M. Goodson,² Eduard Y. Chekmenev^{1,3}

¹ Department of Chemistry, ³ Karmanos Cancer Institute (KCI), Integrative Biosciences (Ibio), Wayne State University, Detroit, Michigan, USA

² School of Chemical & Biomolecular Sciences, Materials Technology Center, Southern Illinois University, Carbondale, Illinois, USA

Introduction: NMR hyperpolarization enhances the detection sensitivity of magnetic resonance by 4-6 orders of magnitude. As a result, it becomes possible to perform *in vivo* detection of dilute hyperpolarized biocompatible molecules and hyperpolarized products of their metabolic transformation. Hyperpolarized [$1\text{-}^{13}\text{C}$]pyruvate is the key injectable hyperpolarized contrast agent currently, and it is under evaluation in over 30 clinical trials registered with clinicaltrials.gov. Hyperpolarized [$1\text{-}^{13}\text{C}$]pyruvate and other ^{13}C - and ^{15}N - hyperpolarized biocompatible molecules are currently produced via dissolution Dynamic Nuclear Polarization (d-DNP). However, d-DNP instrumentation has high cost and requires a long time (1h) to hyperpolarize [$1\text{-}^{13}\text{C}$]pyruvate and other ^{13}C - and ^{15}N - biocompatible contrast agents. Faster and more cost-effective technologies are needed for hyperpolarization of [$1\text{-}^{13}\text{C}$]pyruvate and other ^{13}C - and ^{15}N - biocompatible contrast agents to enable their routine clinical use in a manner similar to that of PET tracers.

Results and Conclusion: Here, a next-generation clinical-scale parahydrogen-based hyperpolarizer and other auxiliary instrumentation is presented to enable efficient hyperpolarization of [$1\text{-}^{13}\text{C}$]pyruvate and other ^{13}C - and ^{15}N - biocompatible contrast agents. Order-unity ^{13}C polarization of [$1\text{-}^{13}\text{C}$]pyruvate (and structurally similar biomolecules such as α -ketoglutarate and α -keto-[$1\text{-}^{13}\text{C}$]isocaproate) in seconds becomes possible via SABRE-SHEATH (SABRE in SHield Enables Alignment Transfer to Heteronuclei) using this equipment. SABRE-SHEATH relies on non-hydrogenative use of parahydrogen gas that performs simultaneous exchange with to-be-hyperpolarized substrates in microtesla magnetic fields. Moreover, ^{15}N hyperpolarization of [$^{15}\text{N}_3$]metronidazole (FDA-approved antibiotic and potential hypoxia sensor) in excess of 20% is demonstrated using this hyperpolarizer. The device has a footprint of $18.5'' \times 24'' \times 18.5''$ with the cost of the off-shelf components of less than \$15,000 (ca. 2020).

Although the field of parahydrogen-based hyperpolarization techniques has enjoyed a recent revival, the entry barrier to the field remains relatively high due to high cost (\$0.1M) and complex siting of clinical-scale parahydrogen generators capable of producing near 100% parahydrogen. Here, we present on the development and validation of a handheld disposable container for temporary parahydrogen storage and utilization. This solution has the potential of enabling convenient access to parahydrogen for research sites that do not have established infrastructure in pre-clinical and clinical setting. We envision this disposable container to provide a dose of parahydrogen gas to enable a clinical-scale production of parahydrogen-based hyperpolarized contrast agents such as [$1\text{-}^{13}\text{C}$]pyruvate and others. As a result, one parahydrogen generator can potentially support tens of clinical sites for on-site production of hyperpolarized contrast agents using parahydrogen-based hyperpolarization.

As a proof of principle, we demonstrate the utility of this disposable storage container to store a mixture of parahydrogen and propylene gases: the exponential parahydrogen decay T_1 contrast was 6.0 ± 0.5 days. This approach allowed us to transport the parahydrogen/propylene gas mixture over a distance that is >100 -mile to a clinical site operating a 3T MRI scanner. Hyperpolarized propane was produced by ejecting the parahydrogen/propylene gas mixture through a disposable handheld non-magnetic propane hyperpolarizer next to the MRI scanner. The mixture reacts with a heterogeneous Rh/TiO₂ catalyst to produce a pure (from catalyst) batch of hyperpolarized propane gas. The clinical-scale production of parahydrogen-hyperpolarized propane gas was visualized in phantoms using GRE, FIESTA, and EPI pulse sequences without any modification of the clinical scanner sequences or hardware. The presented approach potentially enables on-demand clinical-scale production of hyperpolarized propane (FDA-approved gas for unlimited use in foods) for potential applications as an inhalable contrast agent for pulmonary imaging.

Conclusion: The presented instrumentation developed through multi-team collaboration bodes well for future clinical translation of hyperpolarized contrast agents.

References: (1) Nantogma, S.; Joalland, B.; Wilkens, K.; Chekmenev, E. Y. Clinical-Scale Production of Nearly Pure ($>98.5\%$) Parahydrogen and Quantification by Benchtop NMR Spectroscopy. *Anal. Chem.* **2021**, 93, 3594. (2) Joalland, B.; Nantogma, S.; Chowdhury, M. R. H.; Nikolaou, P.; Chekmenev, E. Y. Magnetic Shielding of Parahydrogen Hyperpolarization Experiments for the Masses. *Magn. Reson. Chem.* **2021**, 59, 1180. (3) Adelabu, I.; TomHon, P.; Kabir, M. S. H.; Nantogma, S.; Abdulmojeed, M.; Mandzhieva, I.; Ettedgui, J.; Swenson, R. E.; Krishna, M. C.; Theis, T., et al. Order-Unity ^{13}C Nuclear Polarization of [$1\text{-}^{13}\text{C}$]Pyruvate in Seconds and the Interplay of Water and SABRE Enhancement. *ChemPhysChem* **2022**, 23, 131. (4) TomHon, P.; Abdulmojeed, M.; Adelabu, I.; Nantogma, S.; Kabir, M. S. H.; Lehmkuhl, S.; Chekmenev, E. Y.; Theis, T. Temperature Cycling Enables Efficient ^{13}C SABRE-SHEATH Hyperpolarization and Imaging of [$1\text{-}^{13}\text{C}$]-Pyruvate. *J. Am. Chem. Soc.* **2022**, 144 (1), 282–287. (5) Theis, T.; Truong, M. L.; Coffey, A. M.; Shchepin, R. V.; Waddell, K. W.; Shi, F.; Goodson, B. M.; Warren, W. S.; Chekmenev, E. Y. Microtesla SABRE Enables 10% Nitrogen-15 Nuclear Spin Polarization. *J. Am. Chem. Soc.* **2015**, 137 (4), 1404-1407.

Acknowledgements: NSF CHE-1905341 and CHE-1904780, NHLBI R21HL154032 and F32HL160108, NIBIB 1R01EB029829, CDMRP W81XWH-20-10576 and W81XWH-20-10578.

Metabolic Signatures in High Grade Serous Ovarian Cancer (HGSOC)

Ming Li Chia¹, Susana Ros¹, Alan Wright¹, Flaviu Bulat^{1,2}, Adam Gaunt¹, Maria Vias¹, Evis Sala⁵, James Brenton^{1,3,5}, Kevin Brindle^{1,4}
University of Cambridge, United Kingdom: ¹Cancer Research UK Cambridge Institute, ²Department of Chemistry, ³Department of Oncology, ⁴Department of Biochemistry, ⁵Cambridge University Hospital, Addenbrooke's Hospital

Introduction: Long-term survival in late-stage Ovarian Cancer has shown only modest improvements over the last four decades [1]. Metabolic imaging with hyperpolarized ¹³C-labelled substrates is a promising technique for imaging tissue metabolism in vivo [2]. Positron emission tomography (PET) measurements of the uptake of the glucose analogue 2-deoxy-2-[fluorine-18]fluoro-D-glucose (¹⁸F-FDG) are already widely used in the clinic. HGSOC is classified into 7 copy number signatures which result in differences in signalling pathways[3]. It is plausible that we might identify metabolic differences between the signatures. An ongoing study at Addenbrooke's Hospital has demonstrated the feasibility of the hyperpolarized ¹³C pyruvate imaging technique in ovarian cancer for detecting early treatment response to neoadjuvant chemotherapy. There are several critical questions that could help accelerate progress in the clinic that this project aims to address: Is there metabolic heterogeneity in different types of HGSOC and how does this correlate with genetic heterogeneity? Could this potentially distinctive metabolism help to predict treatment response?

Methods: *Generation of patient derived xenograft (PDXs) Models:* 3 HGSOC animal models were derived from ascites of stage 3-4 HGSOC patients. They were maintained as patient derived organoid (PDO) lines, representing different copy number signatures[3], and PDOs 1, 2 and 5 were implanted subcutaneously into NOD SCID gamma (NSG) female mice and imaged using the following techniques: *Hyperpolarized [1-¹³C]pyruvate Imaging:* Following injection of 0.3 mL, 82 mM Hyperpolarized [1-¹³C]pyruvate spectra were acquired every second for 3 minutes using surface-coil localized ¹³C MR spectroscopy at 7 T. *¹⁸F FDG PET Imaging:* Following injection of 12-17 MBq [¹⁸F]FDG-glucose, SUV_{max} was measured at 90 minutes. *Dynamic Contrast Enhanced (DCE) MRI:* T₁-weighted ¹H images were acquired for 45 minutes after the injection of 0.2mL, 20mM Dotarem. *²H MRI:* Production of [2,3-²H]malate, following injection of [2,3-²H]fumarate (1 g/kg) was measured using surface-coil localized ²H MR spectroscopy at 7 T. *Diffusion Weighted MRI:* Diffusion-weighted ¹H images were acquired at 9.4 T. *Treatment:* We treated PDO 2 model (carboplatin sensitive) and PDO 5 model (Carboplatin resistant) with i.v. Carboplatin (50mg/kg) or vehicle 1x per week and performed imaging at the following time points: baseline, post treatment at 24 hours, 7 days and weekly thereafter.

Results: *Baseline imaging:* At baseline, we have analyzed the glycolytic state of 3 HGSOC patient derived organoid (PDO) models 1,2 and 5 using hyperpolarized [1-¹³C]-pyruvate MRSI (Fig. 1a), ¹⁸F FDG PET (Fig. 3a) and assessed perfusion using dynamic contrast enhanced (DCE, Fig. 2) MRI. PDOs 1 and 5 showed increased lactate labelling independent of tumour volume compared to PDO 2 , with an average lactate/ pyruvate ratio (LP ratio) of 1.41 ± 0.148 (PDO 1), 0.779 ± 0.111 (PDO2) and 1.43 ± 0.175 (PDO 5) respectively(Fig. 1a). We could not detect any significant differences in [¹⁸F]FDG uptake, calculated as SUV_{max} (Fig. 3a), in these 3 models. [¹⁸F]FDG uptake did not correlate with tumour volume. There was no significant difference in perfusion between the 3 models as determined by DCE MRI (Fig. 2). *Treatment response imaging:* In the clinic, HGSOC is treated with a combination of platinum and taxane based therapy [4]. In the PDO 2 model preliminary data suggest a decrease in lactate labelling from hyperpolarized [1-¹³C]pyruvate at week 4 post-treatment whereas there was no change in tumor volume (Fig. 1b).There was a decrease in SUVmax from baseline at 1 week post treatment for the PDO 2 model before any tumour volume change (control group mean -0.169 ± 0.033 vs treatment group mean -0.554 ± 0.131 , Fig.3b). PDO 5 model showed no significant changes in SUV max from baseline (1 week time point: control group mean 0.098 ± 0.242 vs treatment group mean 0.058 ± 0.016 , Fig. 3c). For both diffusion weighted imaging and ²H-labeled fumarate MRI, there were no significant changes up to week 2 post treatment between the control and treatment groups. **Discussion:** PDO 1 model (Signature 1 which is predictive of poor outcome and platinum resistant relapse) and PDO 5 (Carboplatin resistant model) showed higher lactate labelling than PDO 2. When the tumour extracts were analyzed, heterogeneity in glycolytic enzyme and protein expression was demonstrated between HGSOC organoid models which corresponded to the imaging data. The differences in lactate labelling are likely due to induction of lactate dehydrogenase by c-Myc (PDO 1 vs 2) and EGFR amplification (PDO 5 vs 2). The decrease in FDG uptake and lactate labelling in the post treatment group were shown to correlate with depletion of the NAD(H) pool and increased expression of yH2AX, CC3 and TUNEL staining at week 3-4 post treatment in the treatment group. **Conclusion:** Hyperpolarized [1-¹³C]pyruvate shows promise for metabolic imaging in HGSOC. There is metabolic heterogeneity in the different preclinical models of HGSOC which correlates with genetic heterogeneity. This distinctive metabolism may potentially be used to distinguish between different disease subtypes and to detect their early responses to treatment.

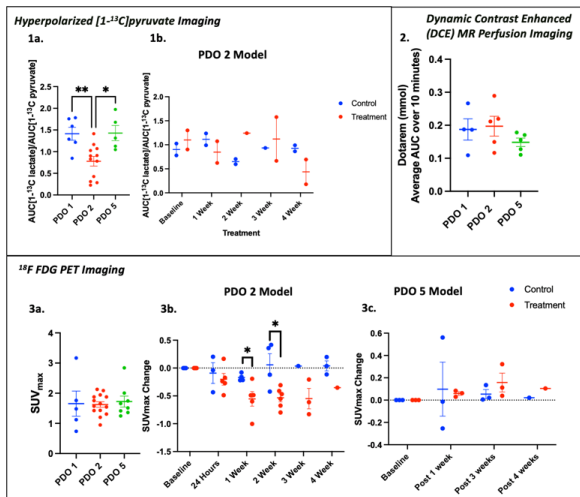


Figure 1. Hyperpolarized [1-¹³C]pyruvate imaging. **a)** Ratio of the area under the lactate and pyruvate labelling curves (AUC). Statistical differences: P=0.0089 (PDO 1 vs 2**), P=0.0119

(PDO 2 vs 5 *), one way anova test. **b)** Carboplatin treatment response. Ratio of AUC in treated and control mice. **Figure 2.**

DCE Imaging. Average AUC of Dotarem over 10 minutes.

Figure 3. ¹⁸F FDG-PET Imaging. **a)** SUV_{max} of tumour 90 minutes following i.v. injection of [¹⁸F]FDG. Carboplatin treatment response. SUV_{max} change from baseline in treated and control mice in **b**) PDO 2 (carboplatin sensitive model) and **c**) PDO 5 (carboplatin resistant model). Control vs treatment group at week 1*, P=0.0384, week 2*, P=0.0117, unpaired t test.

References: 1. Zhang et al., Global patterns and trends in ovarian cancer incidence: age, period and birth cohort analysis. BMC Cancer, 2019.2. Golman et al., Real-time metabolic imaging. Proceedings of the National Academy of Sciences, 2006.3. Macintyre et al., Copy number signatures and mutational processes in ovarian carcinoma. Nature Genetics, 2018.4.NICE, Managing advanced (stage II-IV) ovarian cancer 2020

Extracellular Lactate Imaging with a New Generation of Lanthanide-based Shift Reagents and CEST MRI

Remy Chiaffarelli¹, Paul Jurek³, Garry Kiefer³, André F. Martins^{1,2}

¹ Werner Siemens Imaging Center, Department of Preclinical Imaging and Radiopharmacy, University Hospital Tuebingen, Tuebingen, Germany.

² Cluster of Excellence iFIT (EXC 2180) "Image-Guided and Functionally Instructed Tumor Therapies", University of Tübingen, Germany. ³ Macrocylics, Inc., Dallas, Texas, USA.

Introduction: Cancer cells overproduce lactate even in the presence of high oxygen and glucose levels—Warburg effect. Most of the lactate produced by cancer cells builds up in the extracellular environment. Hence, a method for imaging extracellular lactate produced by the tumors is of utmost importance. Previous reports showed that extracellular lactate could be detected using a paraCEST shift reagent (SR), EuDO3A¹, that binds lactate and shifts its OH-CEST signal away from the water signal. We report here the first results of a new generation of SRs, Eu-, Pr- and YbPCTA, able to image extracellular lactate by CEST MRI with improved kinetic inertness.² **Methods:** Phantoms containing Eu-, Pr- and YbPCTA dissolved in water or serum in the presence/absence of lactate (5–40 mM) were imaged in a 7 T preclinical MR scanner (Bruker Biospec 70/30) using an established CEST FISP sequence and different sets of pre-saturation pulses, to generate CEST spectra and lactate-SRs calibration curves. Exchange rates were calculated using the Omega plot method. r_1 and r_2 values of the SRs were calculated from T_1 and T_2 maps. Structural chemical analysis of the lactate-SR complexes was performed with high-resolution ¹H and ¹³C NMR recorded on a Bruker AVANCE III 400 NMR (9.4 T) spectrometer. Phantoms containing cell culture supernatants and SRs were acquired with the same protocols to detect lactate excreted by MC-38 cancer cells. The selectivity for extracellular lactate and quantification of extracellular lactate present in supernatants from MC-38 cancer cells was assessed *in vitro* by mass spectrometry (LC-MS), CEST phantoms, and lactate LDH assay kits. **Results/Discussion:** Here, we report that Eu-, Pr- and YbPCTA complexes are able to shift the lactate –OH CEST signal to frequencies easily detectable by CEST MRI. (Fig. 1B) All the three lanthanide complexes demonstrated remarkable capabilities to shift lactate OH-CEST signal far away from the water protons. Lactate-YbPCTA complex displays a larger chemical shift (> 95 ppm) compared to EuPCTA (10-18 ppm) and PrPCTA (-5 ppm). High-resolution ¹H NMR confirmed the presence of a major SAP lactate-SR diastereomer in solution for the lactate-YbPCTA complex. Titrations of the SRs with lactate showed a perfect correlation between lactate concentration and CEST signals produced by Eu- and Yb- complexes at neutral and acidic pH (Fig. 1C). The potential of the SRs was demonstrated by quantifying the extracellular lactate produced by MC-38 cells growing in cell culture (Eu- and YbPCTA). The chemical shifts produced by Eu- and YbPCTA-lactate are large enough to exclude any possible interference from the water and other endogenous CEST signals. LDH assays confirmed the high accuracy of extracellular lactate detection by the Ln-PCTA complexes. It is worth noting that the smaller –OH chemical shift produced by PrPCTA and the required high saturation powers ($k_{ex} = 3294 \pm 400 \text{ s}^{-1}$) precluded a precise detection of lactate via CEST imaging due to a significant CEST overlap with water and NOE contributions. Nevertheless, the capability to detect lactate even in potentially confounding OH- and NH- resonances was successfully tested by CEST MRI using the cell culture supernatants. **Conclusion:** In sum, we demonstrated for the first time that alternative lanthanide-PCTA complexes can successfully be used to detect extracellular lactate by CEST MR imaging. The superior kinetic inertness and thermodynamic stability of the Ln-PCTA complexes make them optimal candidates for safe translational imaging studies. These results provide the framework to develop and characterize new SRs to image extracellular lactate produced in tumours by non-invasive CEST MRI.

References: [1] Zhang, L., et al., Imaging Extracellular Lactate In Vitro and In Vivo Using CEST MRI and a Paramagnetic Shift Reagent. *Chemistry*, 2017. 23(8): p. 1752-1756. [2] Rojas-Quijano, F.A., et al., Lanthanide(III) complexes of tris(amide) PCTA derivatives as potential bimodal magnetic resonance and optical imaging agents. *Chemistry*, 2009. 15(47): p. 13188-200.

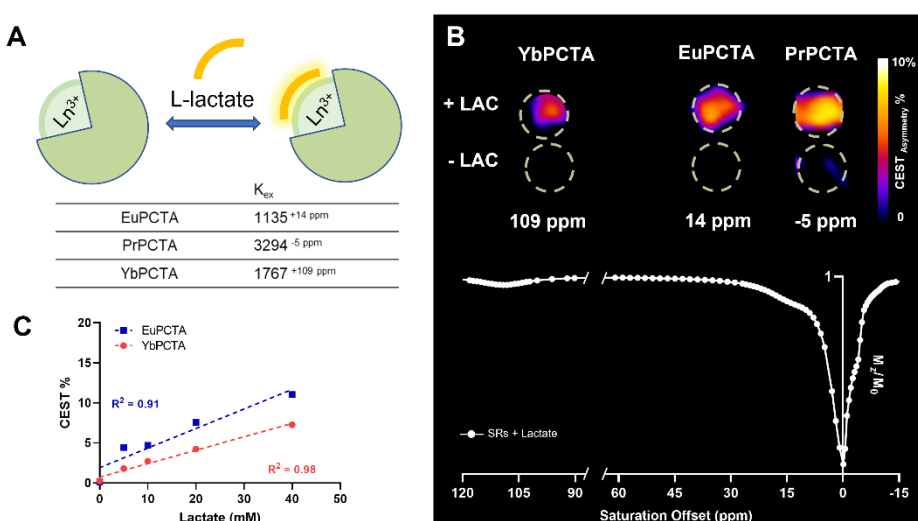


Figure 1. (A) Schematic of lactate-SRs binding and exchange rates (K_{ex}) at pH 7. (B, top) CEST images of phantoms containing 20 mM SRs (-LAC) or 1:1 solutions of SRs and lactate (+LAC) at pH 7, using 5 seconds, 16 μT saturation pulses. (B, bottom) Z-spectrum, showing CEST signal of 20 mM lactate-SR complexes at 109 ppm (Yb-), 14 ppm (Eu-), -5 ppm (PrPCTA). Data were fitted to Lorentzian shapes based on a two-pool model (water, lactate). (C) Plot of CEST effect at 109 ppm (YbPCTA) or 14 ppm (EuPCTA) versus lactate concentration. Dotted lines: linear regression analysis.

Hybrid visualization of cancer acidosis by non-invasive shift/acidoCEST MRI: The S2WTP3 vs. ML1B1B1 invasion quest.

Anaïs Choffart¹, Remy Chiiffarelli¹, Sabrina H.L. Hoffmann¹, André F. Martins^{1,2}

¹Werner Siemens Imaging Center, Department of Preclinical Imaging, University Hospital of Tübingen, Tübingen, Germany

²Cluster of Excellence iFIT (EXC 2180) “Image-Guided and Functionally Instructed Tumor Therapies”, University of Tübingen, Germany.

Introduction: Tumor cells usually show a hyperglycolytic metabolic phenotype with higher lactate production – the Warburg effect. This drift on the oxidative metabolism often leads to a more acidic microenvironment. Iopamidol is a contrast agent used to measure extracellular pH (pH_e) *in vivo* with Chemical Exchange Saturation Transfer (acidoCEST) Magnetic Resonance Imaging (MRI).¹ Moreover, extracellular lactate (lactate_e) can also be detected by CEST (shiftCEST) using a shift reagent (SR).² In this work, we used two murine MMTV-PyVmT-derived cell lines, a parental S2WTP3, and a bone-tropic metastatic ML1B1B1 derived from repetitive *in vivo* selection. Preliminary experiments demonstrated that the two cell lines showed different invasive phenotypes (fig. 1A) and expression patterns of critical metabolic transporters responsible for the regulation of acidosis in the extracellular space. Thus in this study, we aimed at assessing acidification and lactate secretion of the S2WTP3 (parental) and ML1B1B1 (metastatic) with innovative MRI CEST. Here, we report the first results of combining acidoCEST with shiftCEST to determine both pH_e and extracellular lactate with simultaneous application of iopamidol and SR.

Methods: **In vitro spheroid invasion assay:** Spheroids were generated with 1,000 cells via the hanging drop method. The invasive phenotype was assessed on day 7 after the transfer of the spheroid in a 2.5mg/mL collagen gel. **Seahorse assay:** 10,000 cells were analyzed following the Agilent™ “ATP Rate Assay” protocol. **CEST MRI:** 100,000 cells were seeded on 6 well plates for 72h. After 24h, the medium was changed for Agilent™ medium (lower buffer capacity) and incubated in a CO₂-free incubator for 48h before imaging. The supernatant was collected, and different CEST spectra were acquired using 10mM SR and 40mM iopamidol in the presence of the different supernatant on a 7T preclinical MR scanner (Bruker Biospec 70/30) using established CEST FISP sequences. CEST acquisitions were performed using 3µT and 6 seconds continuous saturation pulses or 14µT and 5 seconds continuous saturation pulses, for acidoCEST or shiftCEST, respectively. An LDH assay cross-validated the extracellular lactate concentrations. The pH was confirmed by measurement with a seven compact micro pH meter from Mettler-Toledo.

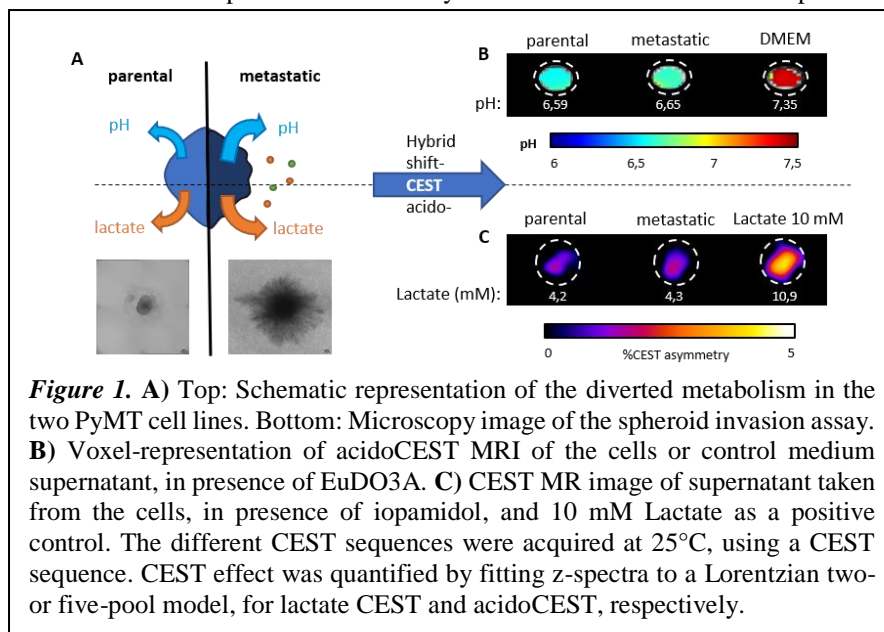


Figure 1. **A)** Top: Schematic representation of the diverted metabolism in the two PyMT cell lines. Bottom: Microscopy image of the spheroid invasion assay. **B)** Voxel-representation of acidoCEST MRI of the cells or control medium supernatant, in presence of EuDO3A. **C)** CEST MR image of supernatant taken from the cells, in presence of iopamidol, and 10 mM Lactate as a positive control. The different CEST sequences were acquired at 25°C, using a CEST sequence. CEST effect was quantified by fitting z-spectra to a Lorentzian two- or five-pool model, for lactate CEST and acidoCEST, respectively.

and MCT1 play a key role in these two different phenotypes. CAIX and MCT1 show significantly higher expression values in the ML1B1B1 cell line ($p<0.0001$). These transporters are strongly associated with acidosis and lactosis in the tumor microenvironment (TME).^{3,4} Following these first studies, we aimed to determine acidosis and lactosis with a non-invasive MR imaging technique by combining shift- and acidoCEST in a single scanning event. Results showed that shift/acidoCEST allowed for determination of pH and extracellular lactate with high accuracy for both ML1B1B1 ($pH = 6.66 \pm 0.02$, $[lactate]_e = 2.402 \pm 0.84$ mM/ 10^6 cells) and S2WTP3 ($pH = 6.587 \pm 0.004$, $[lactate]_e = 1.607 \pm 0.54$ mM/ 10^6 cells). The pH values did not show statistical significance in both measures with CEST, but data indicated a stronger extracellular lactate production for the metastatic cell line. This meager acidification difference is explained by the larger mitochondrial ATP production rate observed for the metastatic cell line—diverted metabolic fitness. We validated the acido/shiftCEST imaging results with direct pH measures using a pH meter and a lactate assay kit, which showed perfect metabolic correlations ($R^2 = 0.93$ and $R^2 = 0.96$, respectively).

Conclusion: In sum, our results show that acido/shiftCEST can be used as a reliable technique for metabolic imaging detecting acidity and extracellular lactate production non-invasively by MRI. We demonstrated for the first time that lactate_e and pH_e could be determined in a single event for two murine PyMT cell lines. This work offers a unique platform for assessing cancer metabolic aggressiveness, provided that acidity and lactate production are critical cancer biomarkers. Hence, acido/shiftCEST shows great potential for future *in vivo* hybrid characterization of the TME.

References: **1.** Moon BF, Jones KM, Chen LQ, et al. A comparison of iopromide and iopamidol, two acidoCEST MRI contrast media that measure tumor extracellular pH. *Contrast Media Mol Imaging*. 2015;10(6):446-455. **2.** Zhang L, Martins A, Mai Y, et al. Imaging extracellular lactate *in vitro* and *in vivo* using CEST MRI and a paramagnetic shift reagent. *Chem Wein Bergstr Ger*. 2017;23(8):1752-1756. **3.** Andreucci E, Peppicelli S, Carta F, et al. Carbonic anhydrase IX inhibition affects viability of cancer cells adapted to extracellular acidosis. *J Mol Med Berl Ger*. 2017;95(12):1341-1353. **4.** Curry JM, Tuluc M, Whitaker-Menezes D, et al. Cancer metabolism, stemness and tumor recurrence. *Cell Cycle*. 2013;12(9):1371-1384.

Results/Discussion: We have recorded CEST using phantoms containing the solutions of iopamidol and SR combined. CEST data recorded in these phantoms showed no difference quantifying both pH and extracellular lactate *in vitro* compared to the agents alone at the same concentrations. Calibration curves with iopamidol and SR showed a strong correlation ($R^2 > 0.98$). To validate our hybrid methodology, we have selected S2WTP3 and ML1B1B1 cell lines for their clear phenotypic differences. An invasion collagen-based assay demonstrated a more invasive profile with the bone-tropic metastatic cell line ML1B1B1 (Fig. 1A). Furthermore, a Seahorse ATP Rate assay showed a stronger ATP production for ML1B1B1 ($p < 0.0001$). Data also show variations in metabolic biomarkers as assessed by western blot and qPCR analysis. For instance, we have observed that CAIX

A hydrogen peroxide sensitive Co(II) lipoCEST agent

Md Saiful I. Chowdhury¹, Janet R. Morrow¹

¹Chemistry Department, The State University of New York at Buffalo, New York, USA

Introduction: Paramagnetic lipoCEST agents are one of the most sensitive CEST (Chemical Exchange Saturation Transfer) agents for MRI (Magnetic Resonance Imaging) being studied now-a-days.¹ Paramagnetic water proton shift agents (SA) are encapsulated inside the liposomal core. Oftentimes, amphiphilic paramagnetic SA is also included in the lipid bilayer of the liposomes. These liposomes are called lipoCEST agents and can be utilized for MR imaging when suspended in isotonic media. However, responsive and targeted lipoCEST agent development is still a challenge to the researchers in this field. In this study, we will present an approach to visualize CEST signal shift upon oxidation of encapsulated core SA to sense peroxide.

Methods: Synthesis: The aqueous soluble SA, Co(II)TPT used in this lipoCEST agent has been synthesized and reported previously.² This SA is a Co(II) complex of 1,4,7-Triazacyclononane (TACN) macrocycle with pyrazole pendants. It has a redox potential of -120 mV versus NHE. This lipoCEST agent also has an amphiphilic SA in its lipid bilayer. This amphiphilic SA is a Co(II) complex of 1,4,8,11-tetraazacyclotetradecane (CYCLAM) macrocycle derivative. Cyclam amines are alkylated to produce three hydroxypropyl-based pendants and one long chain for bilayer integration. This complex has a higher redox potential and does not get oxidized to any large extent in the presence of hydrogen peroxide. Liposome was made of 40 mM lipids (DPPC : DSPE-PEG :

Amphiphilic SA : Cholesterol = 64:6:15:15.) and 40 mM Co(II)TPT for hydration. It was then extruded to 100 nm, sonicated, subjected to ultra-filtration at 100 kDa cut-off and osmotically shrunken in media of 300 and 900 mOsm using NaCl solution to make it ready for imaging. **In-vitro Imaging:** The 'Z' spectra were collected on a 400 MHz NMR spectrometer. Asymmetry from these 'Z' spectra was calculated to extract the saturation transfer peak. The 'Z' spectra are shown at different saturation powers in the figure at 900 mOsm. The CEST peaks were compared to observe a shift upon oxidation in presence of H₂O₂. Control samples were prepared to fit and analyze the CEST data.

Results: Treatment of the lipoCEST agent with an equivalent of H₂O₂ (vs Co(II)TPT) shows a shift of the peak in asymmetry graph after 30 minutes of incubation. Excess H₂O₂ concentration slowly leads to an absence of CEST due to additional lipid bilayer amphiphilic SA oxidation. Concentration of encapsulated Co(II)TPT inside liposome was calculated using UV-vis spectrometry after ultra-filtration (5-10 mM). CEST from H₂O₂ itself in presence of blank liposomes was fitted and subtracted. Diffusion kinetics and oxidation rate kinetics will be reported.

Discussion: Inside liposomes, H₂O₂ can selectively oxidize paramagnetic metal complexes when their redox potentials are properly tuned. Combining this with an amphiphilic SA produces a responsive probe.

Conclusion: H₂O₂ can penetrate liposomal membranes effectively. In case of tumors and inflammation, responsive lipoCEST may be a promising way to study pathology related to these diseases.

Reference:

1. Hancu, I.; Dixon, W. T.; Woods, M.; Vinogradov, E.; Sherry, A. D.; Lenkinski, R. E., CEST and PARACEST MR contrast agents. *Acta Radiol.* **2010**, *51* (8), 910-923.
2. Tsitovich, P. B.; Spernyak, J. A.; Morrow, J. R., A Redox-Activated MRI Contrast Agent that Switches Between Paramagnetic and Diamagnetic States. *Angewandte Chemie International Edition* **2013**, *52* (52), 13997-14000.

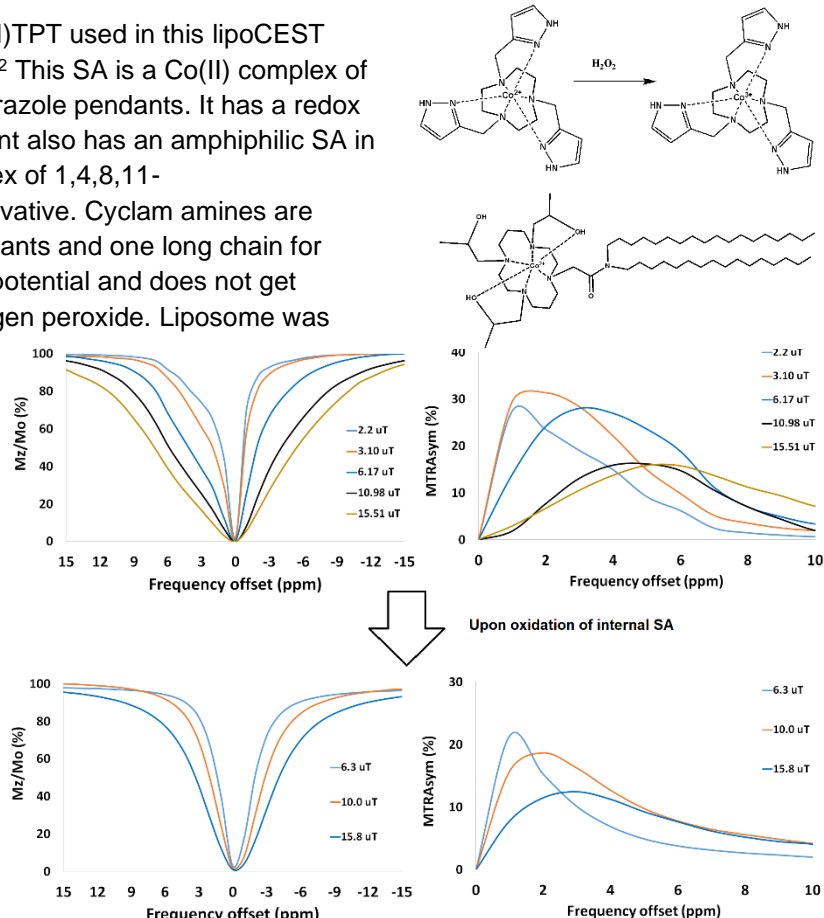


Figure: liposomes containing intraliposomal and amphiphilic SA give Z spectra and asymmetry plot (top). Oxidation with peroxide produces a change in the 'Z' spectra.

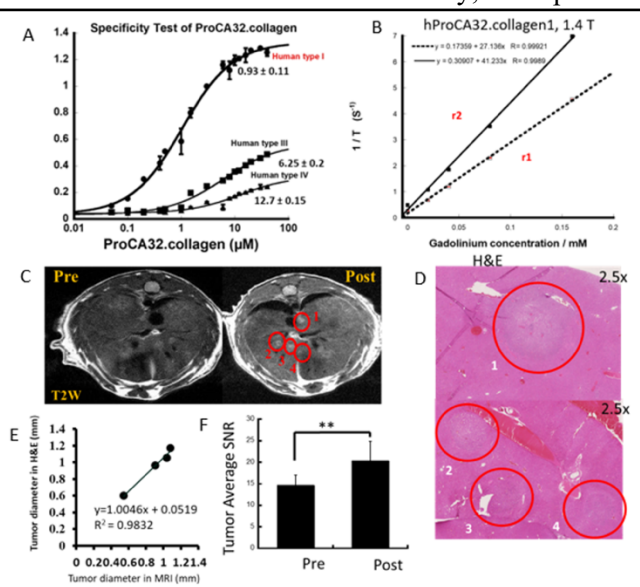
Novel Collagen-targeted Protein MRI Contrast Agent for Noninvasive Detection of Fibrosis and Cancer

Dongjun Li¹, Zongxiang Gui¹, Jingjuan Qiao¹, Brenda-Ruth Mimba¹, Florence N. Reddish¹, Van Ha¹, Odubade Oluwatosin¹, Hua Yang², Khan Hekmateyar¹, Mani Salarian¹, Ravi Chakra³, Zhiren Liu³, Shirong Wang³, Hang Shi³, Bingzhong Xue³, Hans E. Grossniklaus², Jenny J. Yang¹

¹Department of Chemistry, Center for Diagnostics and Therapeutics, Advanced Translational Facility, Georgia State University, Atlanta, GA 30303, USA. ²Department of Ophthalmology, Emory University, Atlanta, GA 30322, USA ³Department of Biology, Georgia State University, Atlanta, GA 30303, USA.

Introduction: Acute and chronic human diseases including liver and lung diseases, cancer, cardiovascular diseases and virus infection, share common key determinants including inflammation and fibrosis. There is a pressing unmet need to facilitate early detection, staging, and treatment responses, by creating non-invasive imaging methodology. The major translational bottle neck is to have cost effective manufactural and formational processes for large scale production.

Results and Conclusion: In this study, we report our recent breakthrough in optimization, characterization, formulation, and production of a set of novel human protein-based contrast agents (ProCA(R)s) pioneered by our team for both preclinical and clinical applications. We have shown that hProCA32.collagen exhibits 6.7-fold and 13.7-fold binding affinity for collagen type 1 than type 3 and 4, respectively. The expression yield for large scale production is largely improved by optimizing fermentation conditions. We have developed an array of functional and quality control assays including ELISA for collagen binding, SEC-HPLC for purity control, RP-HPLC for titer determination, ICP-OES for monitoring stability, mass spectrometry for molecular weight determination, and DLS for aggregation detection. Several production processes and protein formulation conditions were established by controlling protein folding. The newly formulated protein possesses high relaxivities per particle at both 1.4 and 7.0 T and high collagen binding affinity ($K[d]$: 1.0 μM), which enables the robust detection of early-stage liver fibrosis via dual contrast modes. hProCA32.collagen has high Gd(III) binding affinity less than 10[-21] M and up to 15-fold metal selectivity with $r[1]$ and $r[2]$ relaxivity of 27 mM[-1]s[-1] and 41 mM[-1]s[-1] per Gd(III). Our *in vivo* imaging studies and histological analysis revealed that newly formulated hProCA32.collagen enables MR detection of hepatocellular carcinoma (HCC) and liver metastasis as small as 0.1 mm, about 100-fold improvement in sensitivity for cancer detection. It also detects early-stage fibrosis induced by NASH and ASH in several animal models with strong specificity. We are moving forward rapidly for both preclinical and clinical application of our developed contrast agent for various diseases.



Detection of Early-Stage HCC by hProCA32.collagen

Figure 1. A: Binding specificity of hProCA32.collagen to collagen type I, III, and IV. B: Relaxivity of hProCA32.collagen. C: T2 weighted fast spin echo MR imaging of DEN-induced HCC before and 24 hours after injection of hProCA32.collagen. Lesions not detected pre-injection showed up with high enhancement at 24 hours' time point. D: Hematoxylin and eosin stain of the HCC liver showed corresponding tumor detected by the MRI in the similar position. E: The tumor size detected by MRI has a positively linear correlation ($R^2=0.9832$) with histology data. F: After injection of hProCA32.collagen, a significant enhancement of tumor was observed compared to pre injection. (n=4).

ASH in several animal models with strong specificity. We are moving forward rapidly for both preclinical and clinical application of our developed contrast agent for various diseases.

Reference: 1) Yang, Jenny J., et al. "Rational design of protein-based MRI contrast agents." *Journal of the American Chemical Society* 130.29 (2008): 9260-9267. 2) Salarian, Mani, et al. "Early detection and staging of chronic liver diseases with a protein MRI contrast agent." *Nature communications* 10.1 (2019): 1-14. 3) Salarian, Mani, et al. "Precision detection of liver metastasis by collagen-targeted protein MRI contrast agent." *Biomaterials* 224 (2019): 119478. 4) Xue, Shenghui, et al. "Protein MRI contrast agent with unprecedented metal selectivity and sensitivity for liver cancer imaging." *Proceedings of the National Academy of Sciences* 112.21 (2015): 6607-6612. 5) Tan, Shanshan, et al. "Chemokine receptor 4 targeted protein MRI contrast agent for early detection of liver metastases." *Science advances* 6.6 (2020): eaav7504. 6) Turaga, Ravi Chakra, et al. "Rational design of a protein that binds integrin $\alpha\beta 3$ outside the ligand binding site." *Nature communications* 7.1 (2016): 1-11.

Optimization of CEST reporter genes with a genetic programming Protein Optimization Evolving Tool

Or Perlman¹, Alexander R. Bricco², E. Alejandro Castellanos², Iliya Miralavy³, Shaowei Bo⁴, Tyler Gallagher⁵, Leo L. Cheng¹, Michael T. McMahon⁴, Wolfgang Banzhaf³, Hiroshi Nakashima⁵, Assaf A. Gilad^{6,7}, and Christian T. Farrar¹

¹Martinos Center for Biomedical Imaging, Massachusetts General Hospital and Harvard Medical School, Charlestown, MA; ²Department of Biomedical Engineering, Michigan State University, East Lansing, MI; ³Department of Computer Science & Engineering, Michigan State University, East Lansing, MI; ⁵Department of Neurosurgery, Brigham & Women's Hospital, Boston, MA; ⁴Department of Radiology and Radiological Sciences, Johns Hopkins University School of Medicine, Baltimore, MD; ⁶Department of Chemical Engineering and Materials Science, Michigan State University, East Lansing, MI; ⁷Department of Radiology, Michigan State University, East Lansing, MI.

Introduction: Cell and viral based therapeutics hold great promise for revolutionizing the treatment of many diseases. However, the optimization of such biological therapies and assessment of their efficacy depends critically on the ability to monitor the spread and persistence of the therapeutic agent. We have previously demonstrated that a Lysine-Rich Protein (LRP) Chemical Exchange Saturation Transfer (CEST) MRI-based reporter gene¹ can be used for imaging oncolytic virotherapy² as well as cardiac gene transfer therapy³. However, the detection sensitivity was limited, and the reporter gene was not stable due to the highly repetitive nature of the DNA sequence. To optimize the design of CEST reporter proteins we have developed a novel genetic programming algorithm, Protein Optimization Evolving Tool (POET)⁴. Here we characterize CEST peptides optimized using POET and use the best performing peptides to construct new CEST reporter genes.

Methods: POET was used to optimize the design of 12mer CEST peptides to provide maximal CEST contrast at either 3.6 or 5 ppm⁴. Each generation of optimized peptides were synthesized, and the proton Magnetization Transfer Ratio Asymmetry (MTR_{asym}) was experimentally measured on a 7T Bruker MRI scanner. The experimental results were then used to improve the predictive model of the POET. The amide exchange rates and proton volume fractions were quantified using QUESP⁵ on a 14T Bruker NMR spectrometer. The contribution of the different exchangeable proton pools (amide, amine, and hydroxyl) to the overall CEST Z-spectrum was quantified by 4-pool Lorentzian fitting⁶ of the Z-spectra acquired at 14T. Different combinations of the 5 best peptides were then used to generate new optimized reporter genes. Protein structures were predicted using Robetta and the 2 most disordered proteins (ASM1 and ACF2) were selected. Genes encoding these proteins and a P2A tag for western blot detection were engineered into a pcDNA3.1 P2A-eGFP vector and transfected into HEK293 cells. Western blots of HEK293 cell lysates were run to characterize the new reporters.

Results and Discussion: After 10 generations we have obtained a group of peptides with amide CEST contrast up to 4 times greater than poly-L-lysine (K12), the basis for the original LRP reporter protein. Most of the POET optimized peptides showed improvement in the average amide proton exchange rate and amide CEST contrast with some of the peptides demonstrating exchange rates almost 2-times faster than K12 (**Table 1**). Some of the POET optimized peptides had lower amide exchange rates relative to K12, however, the amine CEST contrast at 2 ppm was significantly greater for these peptides indicating that the increased MTR_{asym} at 3.6 ppm for these optimized peptides also has contributions from the amine exchangeable protons. Thus, POET can optimize and exploit both amide and amine protons to maximize the MTR_{asym} at 3.6 ppm. The reporter genes AMS1 and ACF2, consisting of different combinations of the 5 best CEST peptides, were chosen due their predicted disordered structure (**Figure 1, left**), which provides optimal solvent access for the exchangeable protons. Western blots of HEK293 cell lysates (**Figure 1, right**) show a single well-defined band at approximately the correct molecular weight indicating expression of full-length protein and a stable reporter gene. Experiments are currently underway to test the *in vitro* and *in vivo* performance of the optimized reporter genes in tumor cell lines engineered to express the new reporters.

Table 1: Normalized CEST Contrast (%)¹ k_{ex} (Hz)

Peptide Sequence	Amide	Amine	OH	Amide
KKKKKKKKKKKK	2.18	0.04	0.0	423
KPWHGCASRTKR	4.28	4.95	6.41	548
DVKCKIQKRKWH	2.91	1.74	0.0	422
KKRLHWIRWHCG	2.27	4.67	0.0	195
CCWHNPWKRRTR	2.05	5.23	7.19	433
KYTKTRKQSSKA	5.42	2.19	4.71	754
NSSNHSNNMPCQ	5.26	0.91	1.40	822

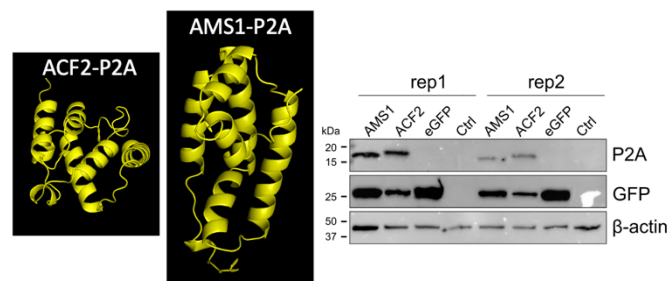


Figure 1: (left) Robetta predicted protein structures of AMS1 and ACF2 reporter proteins; (right) Western blot of HEK293 cell lysates transfected with the reporter genes.

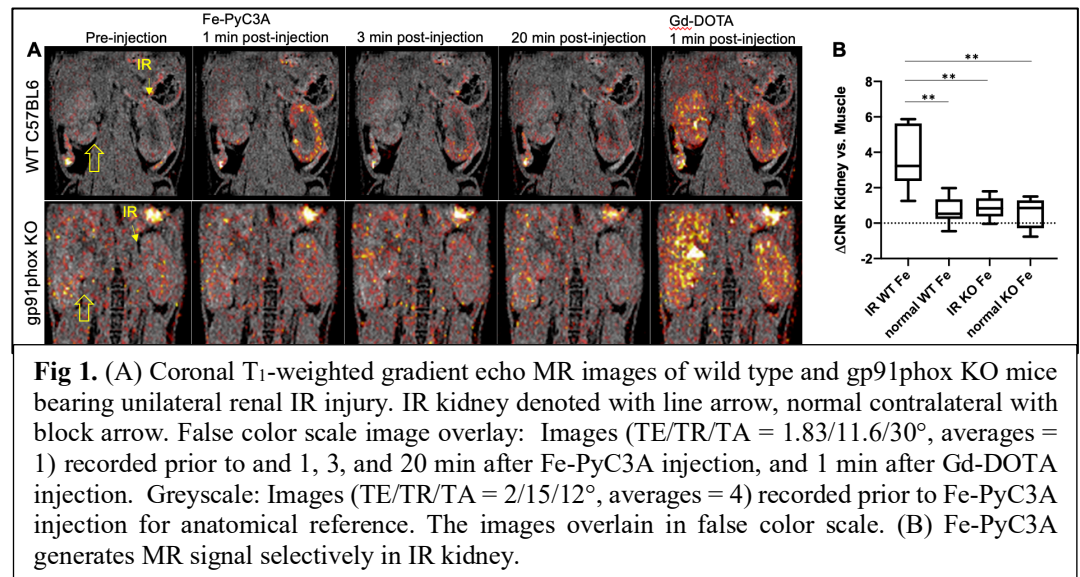
References: 1. Gilad, A. A. et al. *Nat Biotech* 25, 217–219 (2007); 2. Farrar, C. T. et al. *Radiology* 275, 746–754 (2015); 3. Meier, S. et al. *Sci Rep* 8, 4638 (2018); 4. Bricco, A. R. et al. *bioArXiv* (2022) doi:10.1101/2022.03.05.483103; 5. McMahon, M. T. et al. *Magn Reson Med* 55, 836–847 (2006); 6. Zaiss, M., Schmitt, B. & Bachert, P. *J Magn Reson* 211, 149–155 (2011).

Precision Magnetic Resonance Imaging of Kidney Inflammation

Mozhdeh Sojoodi,¹ Ivy Rosales,² Ilknur Ay,³ Kenneth K. Tanabe,¹ Peter Caravan,³ Veronica Clavijo Jordan,³ Iris Yuwen Zhou,³ Eric M. Gale³

Surgical Oncology,¹ Pathology,² and A.A. Martinos Center for Biomedical Imaging and Institute for Innovation in Imaging, Radiology,³ Massachusetts General Hospital, Harvard Medical School.

Introduction: Inflammation is a key driver of numerous kidney disease states related to ischemia, auto-immunity, drug toxicity, and allograft dysfunction, but unfortunately definitive diagnosis of kidney inflammation disease activity requires invasive biopsy. Elevated concentrations of reactive oxygen species (ROS) are a hallmark of the inflammatory microenvironment and thus ROS imaging has been proposed as a non-invasive biomarker of inflammation. The goal of this work is to evaluate the capability of the oxidatively activated MR imaging probe Fe-PyC3A, which upon oxidation changes from the virtually MR silent Fe^{2+} state to the strongly MR visible Fe^{3+} state, to image kidney inflammation in a unilateral mouse model of kidney ischemia reperfusion (IR) injury. **Methods and Materials:** *Imaging probes.* Fe-PyC3A, synthesized as described previously.¹ Gd-DOTA (manufactured by Guerbet) was used as the negative probe. *Mouse models.* Unilateral IR injury was generated via 26 min ligation of the left renal artery of C67BL/6J mice. The mice were imaged one day after IR injury. To confirm the link between Fe-PyC3A generated kidney MR signal increase and inflammation, IR injury and MR imaging were performed on B6.129S-Cybb^{tm1Dn}/J (gp91phox knockout) mice ($n=6$) in which myeloid leukocytes are incapable of respiratory burst. *MR imaging.* Imaging was performed on a 4.7T scanner (Bruker Biospec). Mice were imaged dynamically with a series of 3D T_1 -weighted FLASH sequences prior to and out to 20 minutes after injection of 0.05 mmol/kg Fe-PyC3A ($n=6$). After kidney signal returned to near baseline levels, the mice were again imaged dynamically following injection of a 0.025 mmol/kg Gd-DOTA as non-oxidatively activated negative control probe. *Ex vivo tissue analysis.* After imaging, tubular damages and inflammation were confirmed by H&E stain. Myeloid cell infiltration in IR kidneys was confirmed by IHC staining for myeloperoxidase. *Data analysis.* (Post-pre)injection change in IR and normal kidney vs. muscle contrast-to-noise ratio (ΔCNR) for both WT and gp91phox KO mice were compared by two-way ANOVA followed by Tukey's post-test for multiple comparisons. **Results:** Coronal T_1 w-images recorded prior to and 1, 3, and 20 min after injection of Fe-PyC3A, and 1 min after Gd-DOTA injection to WT and gp91phox KO mice are compared in Figure 1A. Fe-PyC3A provides strong enhancement only in the IR kidney of WT mice. The ΔCNR values recorded in the IR kidney of WT mice 1 min after Fe-PyC3A injection are significantly greater vs. the values recorded the normal contralateral kidney of WT mice ($P = 0.0018$), vs. the IR kidney of gp91phox KO mice ($P = 0.0030$), and vs. the normal contralateral kidney of gp91phox KO mice ($P = 0.0013$), Figure 1B. In contrast, imaging 1 min after Gd-DOTA injection found no significant differences in ΔCNR amongst the IR and contralateral kidneys of both WT and gp91phox KO mice. Fe-PyC3A enhancement of the IR kidney diminishes rapidly, returning to near baseline levels within 20 min post-injection. No significant differences in myeloid cell infiltration are observed in IR kidney from WT and gp91phox KO mice, confirming a robust inflammatory response in both strains (not shown). **Discussion.** Imaging tools to diagnose, quantify, map, and monitor kidney inflammation disease activity are sorely needed. However, the kidney is a technically challenge organ to image with molecularly-targeted probes. Small molecule imaging probes are eliminated by renal filtration resulting in high non-specific background signal in the kidney due to elimination of the unbound probe. Fe-PyC3A is unique in that it generates virtually zero background signal in normal kidney tissue, but is instantaneously oxidized to a strongly MR visible Fe^{3+} complex within the inflammatory kidney microenvironment. Our experiment to image unilateral IR injury in mice clearly demonstrates the how the uncomplicated, inflammation-specific MR signal turn on effect can be applied to image inflammatory disease states of the kidney. The observation that Gd-DOTA generates comparable enhancement in both the normal and IR kidneys underscores the specificity of Fe-PyC3A for the inflammatory microenvironment. Control imaging using gp91phox KO mice, which exhibit a robust inflammatory response in the IR kidney but lack the myeloid cell-ROS secretion machinery, establishes a mechanistic link between kidney Fe-PyC3A response and ROS secreted by inflammatory myeloid cells. **Conclusion:** ROS imaging with Fe-PyC3A represents a potentially powerful non-invasive biomarker for kidney inflammation. **References:** (1) Wang H, Clavijo Jordan V, Ramsay IA, et al. Molecular Magnetic Resonance Imaging Using a Redox-Active Iron Complex. *J. Am. Chem. Soc.* 2019, 141, 5916-5925.



Title: The development of highly water-stable MRI contrast agent sensors for hydrogen peroxide

Introduction: The overproduction of reactive oxygen species, such as H₂O₂, has been connected to a wide array of health conditions. Methods to non-invasively visualize oxidative stress could allow physicians to more swiftly and accurately diagnose a variety of cardiovascular, inflammatory, and neurological disorders. We previously found that Mn(II) complexes with polydentate quinol-containing ligands react with H₂O₂ to yield more highly aquated Mn(II) complexes with oxidized *para*-quinone-containing forms of the ligands that do not chelate the metal ion as effectively.¹⁻³ This chemical reaction thereby increases the *T₁*-weighted relaxivity (*r₁*) of the compounds by as much as 30%. One drawback is that the Mn(II) complexes with the initially explored acyclic ligands are not adequately stable in water, particularly after oxidation.

Methods: We prepare Mn(II) and Fe(II) complexes with a macrocyclic ligand, assess their stabilities to water and air, characterize their response to H₂O₂, and assess their abilities to act as *T₁*-weighted MRI contrast agents before and after oxidation. We use the ligand 1,8-bis(2,5-dihydroxybenzyl)-1,4,8,11-tetraazacyclotetradecane (H₄qp4).⁴

Results and Discussion: We find that the inclusion of the macrocycle markedly improves the stabilities of the complexes, with all relevant log *K_{ML}* values exceeding 18. The macrocycle does so without worsening the *T₁*-weighted response to H₂O₂. To the contrary, we find that the *r₁* of the Mn(II)-H₄qp4 complex increases by 130% upon oxidation by H₂O₂. The Fe(II)-H₄qp4 complex exhibits over a 400% increase in *r₁* upon oxidation, although the absolute magnitude of the change in *r₁* (0.7 mM⁻¹ s⁻¹) is less than the 4.2 mM⁻¹ s⁻¹ observed for the Mn(II)-containing sensor. The response of the Mn(II) complex is correlated to ligand oxidation and an increase in the aquation number. The response of the Fe(II) complex, conversely, is correlated to the oxidation of the metal center to Fe(III). Despite the use of a ligand that can be oxidized to a less highly chelating form, the Fe(III) product does not appear to rapidly exchange water molecules – this keeps the *r₁* of the oxidized sensor at a relatively low value (0.9 mM⁻¹ s⁻¹). Both the Mn(II) and Fe(II) complexes with H₄qp4 display complicated reaction kinetics with H₂O₂ in that a faster rate of sensor oxidation is observed with lower concentrations of H₂O₂. We currently believe that this is due to competing catalase-like activity.

Conclusions: We have developed highly water-stable coordination complexes that can selectively respond to H₂O₂ over O₂ with large percentile increases in *r₁*. The responses of the Mn(II) and Fe(II) compounds result from different underlying mechanisms: improved metal center aquation for the Mn(II) sensor and higher paramagnetism and slower electron spin relaxation for the Fe(II)/Fe(III) system.

References

1. Senft, L.; Moore, J. L.; Franke, A.; Fisher, K. R.; Scheitler, A.; Zahl, A.; Puchta, R.; Fehn, D.; Ison, S.; Sader, S.; Ivanović-Burmazović, I.; Goldsmith, C. R., Quinol-Containing Ligands Enable High Superoxide Dismutase Activity by Modulating Coordination Number, Charge, Oxidation States and Stability of Manganese Complexes throughout Redox Cycling. *Chem. Sci.* **2021**, *12* (31), 10483-10500.
2. Yu, M.; Ambrose, S. L.; Whaley, Z. L.; Fan, S.; Gorden, J. D.; Beyers, R. J.; Schwartz, D. D.; Goldsmith, C. R., A Mononuclear Manganese(II) Complex Demonstrates a Strategy to Simultaneously Image and Treat Oxidative Stress. *J. Am. Chem. Soc.* **2014**, *136*, 12836-12839.
3. Yu, M.; Ward, M. B.; Franke, A.; Ambrose, S. L.; Whaley, Z. L.; Bradford, T. M.; Gorden, J. D.; Beyers, R. J.; Cattley, R. C.; Ivanović-Burmazović, I.; Schwartz, D. D.; Goldsmith, C. R., Adding a Second Quinol to a Redox-Responsive MRI Contrast Agent Improves Its Relaxivity Response to H₂O₂. *Inorg. Chem.* **2017**, *56* (5), 2812-2826.
4. Karbalaei, S.; Knecht, E.; Franke, A.; Zahl, A.; Saunders, A. C.; Pokkuluri, P. R.; Beyers, R. J.; Ivanović-Burmazović, I.; Goldsmith, C. R., A Macroyclic Ligand Framework That Improves Both the Stability and *T₁*-Weighted MRI Response of Quinol-Containing H₂O₂ Sensors. *Inorg. Chem.* **2021**, *60* (12), 8368-8379.

Non-invasive Mapping of molecular determinants for Liver cancer and metastatic aggressiveness by Precision MRI (pMRI)

Zongxiang Gui¹, **Shanshan Tan**¹, **Jingjuan Qiao**¹, **Dongjun Li**¹, **Tosin Ibhangui**¹, **Hua Yang**², **Khan Hekmatyar**¹, **Yuguang Meng**³, **Nan Wang**^{4,5}, **Yibin Xie**⁴, **Phillip Zhe Sun**³, **Ekihiro Seki**⁶, **Debiao Li**^{4,5}, **Hans E. Grossniklaus**², **Jenny J. Yang**¹

¹Department of Chemistry, Advanced Translational Imaging Facility, Center for Diagnostics and Therapeutics, Georgia State University, Atlanta, GA 30303, USA, ²Department of Ophthalmology, Emory University, Atlanta, GA 30322, USA, ³Yerkes National Primate Research Center, Atlanta, GA, 30329, USA, ⁴Biomedical Imaging Research Institute, Cedars-Sinai Medical Center, Los Angeles, CA 90048, USA, ⁵Department of Bioengineering, University of California, Los Angeles, CA 90095, USA, ⁶Department of Medicine, Cedars-Sinai Medical Center, Los Angeles, CA 90048, USA

Introduction: The liver is the most common organ for metastases of various malignancies, especially for pancreatic ductal adenocarcinoma (PDAC), colorectal cancer (CRC), and uveal melanoma (UM). We have found that UM, PDAC, and CRC, share similar pathological growth patterns, suggesting common liver metastasis processes that include formation, predisposition for metastases (pre-met), and formation of pro- and post-metastatic niches for early and late stages of metastasis. Non-alcoholic fatty liver disease (NAFLD) has been reported to significantly increase liver metastasis by orchestrating a pre-metastatic niche with activated hepatic stellate cells (HSCs) and tumor-associated infiltrated immune cells. To date, the detection and characterization of the dynamic changes/interactions of metastasis-associated molecular signatures at multiscale levels are poorly understood. The investigation of the key molecular signatures including chemokine receptor CXCR4, and its interaction with its natural ligand CXCL12 (SDF-1) and fibrotic stroma collagen in regulating the metastasis process largely depends on segmented biochemical and histological approaches that cannot capture heterogeneity and dynamic expression of these molecular biomarkers.

Methods: MRI contrast agent preparation: hProCA32.Collagen / hProCA32.CXCR4 / hProCA32.CXCL12 were expressed, purified and characterized as published protocols. Based on the requirement of agents, pegylation will be modified on the purified Contrast agents². **In-Vivo MRI:** T1- and T2-weighted images, and T1- and T2-mapping were collected before and after one bolus injection of hProCA32.Collagen / hProCA32.CXCR4 / hProCA32.CXCL12 (0.025 mmol/kg) at 3, 24, and 48 hours.

Table. 1. High relaxivities of hProCA32.CXCR4/hProCA32.CXCL12 binds with Gd³⁺ and Mn²⁺

Relaxivities of investigated contrast agents in 10 mM HEPES buffer at 37 °C				
Contrast agent	r_1 (1.4 T)	r_2 (1.4 T)	r_1 (7.0 T)	r_2 (7.0 T)
Gd ³⁺ -ProCA32.CXCR4	30.9 ± 0.5	43.2 ± 1.0	6.67 ± 0.4	51.1 ± 3.2
Gd ³⁺ -ProCA32.CXCL12	27.6 ± 0.9	41.4 ± 2.7	6.70 ± 0.3	53.4 ± 2.2
Mn ²⁺ -ProCA32.CXCR4	18.3 ± 0.5	64.5 ± 1.0	5.96 ± 0.4	127.1 ± 3.2
Mn ²⁺ -ProCA32.CXCL12	17.6 ± 0.9	62.4 ± 2.7	6.05 ± 0.3	131.4 ± 2.2

* Relaxivity values in mM⁻¹ s⁻¹

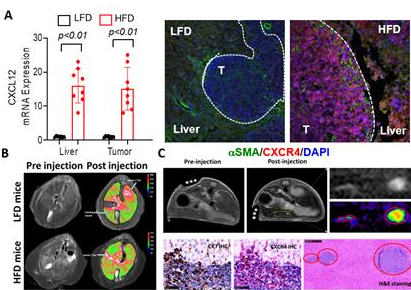


Fig. 1. (A) The expression difference of CXCL12/CXCR4 in LFD/HFD mice model. (B) MRI imaging with hProCA32.CXCL12 in CRC mice model (C) MR image of ovarian cancer mouse model (SK-OV-3) with hProCA32.CXCR4 administration.

Results and Conclusion: In this study, we first demonstrated the chemokine receptor CXCR4, and its interaction with its natural ligand CXCL12 (SDF-1) plays a crucial role in organ specific metastasis progression and outcome. CXCR4 and CXCL12 expression are highly upregulated in liver metastasis and are significantly enhanced in NAFLD. We report the recent development of our pioneered novel class of protein-based MRI contrast agents targeted to CXCR4, CXCL12, and collagen (hProCA32.CXCR4, hProCA32.CXCL12 and hProCA32.collagen) using Precision MRI (pMRI). We also shown that they exhibit high dual relaxivities that are 5-10 folds of Eovist and Multihance at both 1.4T and 7.0T (Table 1). We have demonstrated that hProCA32.CXCR4 and hProCA32.collagen have enabled early detection and stage of liver metastasis from uveal melanoma, ovarian cancer, colon cancer with much-improved sensitivity and specificity compared with non-targeted agents and Eovist^{1,4,5}. Using multitasking methodology with high temporal resolution dynamic imaging of the contrast enhancement process without sacrificing spatial resolution¹, we have demonstrated the rapid detection of liver metastasis of colon cancer with further improved detection sensitivity by overcoming motion artifacts (Fig. 1). The CXCL12 targeted MRI contrast agent (hProCA32.CXCL12) enables the delineation of the micro-vessel (sinusoid space) structure of the liver using pMRI. We discovered that high fat largely alters liver sinusoid structure with a microenvironment pro-metastasis. Further optimizing of our novel imaging methodology and protein contrast agents will provide a comprehensive, longitudinal view of the key determinants of liver metastasis dormancy, progression, and prognosis, and insight into how the imaging tool is useful to understand the mechanism of cancer metastasis in normal and fatty liver. Development of molecular imaging tools and agents will impact subclinical detection, staging, and treatment for metastasis from multiple cancers.

Reference: 1) Xue, S. et al. Protein MRI contrast agent with unprecedented metal selectivity and sensitivity for liver cancer imaging. Proceedings of the National Academy of Sciences 112, 6607-6612 (2015). 2) Yang, Hua, et al. "Non-invasive detection and complementary diagnostic of liver metastases via chemokine receptor 4 imaging." Cancer Gene Therapy (2022): 1-13. 3) Yang, Jenny J., et al. "Rational design of protein-based MRI contrast agents." Journal of the American Chemical Society 130.29 (2008): 9260-9267. 4) Tan, Shanshan, et al. "Chemokine receptor 4 targeted protein MRI contrast agent for early detection of liver metastases." Science advances 6.6 (2020): eaav7504. 5) Salarian, Mani, et al. "Early detection and staging of chronic liver diseases with a protein MRI contrast agent." Nature communications 10.1 (2019): 1-14.

Imaging response to chemo-radiotherapy in glioblastoma tumour models using deuterium metabolic imaging

Friederike Hesse¹, Alan Wright¹, Vencel Somai^{1,2}, Flaviu Bulat^{1,3}, Kevin Brindle^{1,4}

¹ University of Cambridge, CRUK CI, Cambridge, United Kingdom, ² University of Cambridge, Radiology, Cambridge, United Kingdom, ³ University of Cambridge, Chemistry, Cambridge, United Kingdom, ⁴ University of Cambridge, Biochemistry, Cambridge, United Kingdom

Introduction: Cell death is an important imaging target for assessing tumour treatment response and the effectiveness of therapy. In glioblastoma following chemo-radiotherapy (CRT) it can be difficult using conventional imaging techniques to distinguish radio-necrosis, and therefore a positive response to treatment, from disease progression (1). Here we investigated whether deuterium MRI of [2,3-²H]fumarate metabolism can be used to detect tumour cell necrosis (2) in orthotopically implanted radio-sensitive and radio-resistant GBM models and compared these measurements with DWI measurements of tumour cell death. We have shown recently that ²H magnetic resonance spectroscopic imaging can be used to measure the rate of tumor malate production following intravenous injection of [2,3-²H]fumarate (3).

Methods: Serial ²H spectra were acquired from mice implanted orthotopically with patient-derived glioblastoma cells using a fast 3D deuterium MRI pulse sequence with a time resolution of 5 minutes, and a spatial resolution of 3 x 3 x 9 mm³(4) following a bolus injection of [²H] fumarate, before and 48 h after the last treatment with targeted CRT (20 Gy in total with 5Gy/fraction, temozolamide (100 mg/kg)) delivered using a small-animal radiation research platform (SARRP). ²H MR spectroscopy and spectroscopic images were acquired at 7T, and ¹H images at 9.4 T. Diffusion-weighted images were acquired at 9.4 T using a spin echo pulse sequence with echo planar readout (FOV 40 x 40 mm², data matrix 64 x 64; TE 44.86 ms, b-values of 16.17, 56.06, 106.06, 206.06, 406.06 and 806.06 s/mm²).

Results: Surface-coil localized ²H MR spectroscopy and spectroscopic imaging were used to assess conversion of [2,3-²H]fumarate to [2,3-²H]malate in orthotopically implanted GB tumors following an injection of labelled fumarate (1g/kg) into tumor-bearing mice (Figures 1). ²H spectra acquired over 60 minutes at 48 h after the last CRT showed an increase in the malate/fumarate ratio from 0.051 ± 0.03 to 0.22 ± 0.03 ($p=0.04$, $n=3$) in a radioresistant tumor (A11) and from 0.11 ± 0.032 to 0.94 ± 0.05 ($p=0.0006$, $n=3$) in a radiosensitive tumor (S2). Changes in the apparent diffusion coefficient of tissue water were only apparent 7 days after treatment (0.71×10^{-3} to 0.9×10^{-3} mm²/s, $p=0.017$) and only in the radiosensitive S2 model (Figure 2).

Discussion: Malate production, was increased significantly post-treatment after injection of ²H-labeled fumarate. The DW- ¹H MRI experiment, however, showed no change in the median ADC of tumor water over this period and the tumor area on diffusion images remained homogeneous. The ²H-labeled fumarate experiment, therefore, detects diffuse tumor necrosis and so may be a more sensitive measure of necrosis than the DW-MRI experiment (5).

Conclusions: Tumour malate production from [2,3-²H] fumarate increased significantly at 48 h after targeted CRT, demonstrating the potential of ²H-labeled fumarate for distinguishing radio-necrosis (pseudoprogression) from true disease progression. DWI in contrast, only detected response when necrosis was widespread at 7 days post-

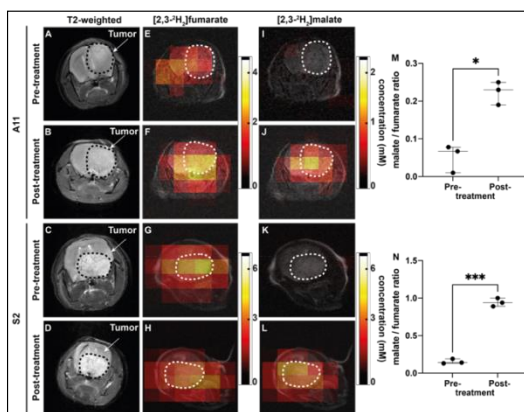


Figure 1: Metabolite concentration maps derived from dynamic 3D chemical shift ²H images summed over 60 min following [2,3-²H]fumarate injection. The colour code represents concentration (in mM) derived from ratios of peak intensities in the malate and fumarate maps to peak intensities in an initial HDO map and corrected for the number of ²H labels per molecule and signal saturation. (A-D) T₂-weighted axial slices. (E-L) Concentration maps of (E,G) fumarate, (I,K) malate pre-treatment; (F,H) fumarate, (J,L) malate 48 h after the last treatment

treatment. The ²H-labeled fumarate experiment, therefore, detects diffuse tumour necrosis and so may be a more sensitive measure of GBM response to chemo-radiation. **References:** (1.) Bonm AV, Ritterbusch R, Throckmorton P, et al. Clinical Imaging for Diagnostic Challenges in the Management of Gliomas: A Review. Journal of neuroimaging : official journal of the American Society of Neuroimaging 2020;30:139-45. (2.) Neves AA, Brindle KM. Imaging cell death. J Nucl Med. 2014;55(1):1-4. (3.) Hesse F, Somai V, Kreis F, et al. Monitoring tumor cell death in murine tumor models using deuterium magnetic resonance spectroscopy and spectroscopic imaging. Proc Natl Acad Sci U S A 2021;118(12). (4.) Kreis F, Wright AJ, Hesse F, et al. Measuring Tumor Glycolytic Flux in Vivo by Using Fast Deuterium MRI. Radiology 2020;294(2):289-296. (5.) Bohndiek SE, Kettunen MI, Hu DE, et al. Detection of tumor response to a vascular disrupting agent by hyperpolarized ¹³C magnetic resonance spectroscopy. Mol Cancer Ther 2010;9(12):3278-3288.

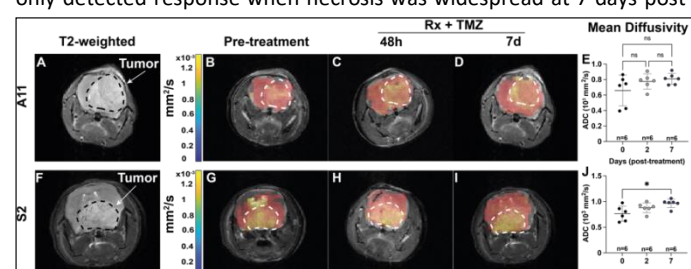


Figure 2: Diffusion-weighted imaging of A11 ($n=6$) and S2 ($n=6$) tumors before and after treatment. (A,F) T₂-weighted axial slices from a reference ¹H image. Representative images before (B,G) and at 24 h (C,H) and 7 d (D,I) after the first CRT treatment. The locations of the tumors are outlined by dotted white lines. (E,J) ADC shows an increase 7d after the last CRT session in S2 tumors (J), but failed to detect changes within 48 h after chemo-radiotherapy treatment.

Cathepsin-Responsive Theranostic Nanoparticles for Image-Guided Glioblastoma Inhibition

Ching-Hsin Huang¹, Edwin Chang^{1,2}, Li Zhang³, Joe Gerald Jesu Raj¹, Laura J. Pisani^{1,4}, and Heike Daldrup-Link¹

¹Molecular Imaging Program, Stanford University, United States; ²Canary Center, Stanford University, United States; ³ChemH, Stanford University, United States; ⁴James H. Clark Center, Stanford University, United States

Introduction: Glioblastoma (GBM) is a highly lethal and difficult-to-treat cancer and chemo-drugs treatment is limited due to their off-target toxicity and low accumulation at GBM. Given that 99% GBM overexpresses cathepsin B,¹ we developed novel theranostic nanoparticles that can be selectively cleaved by cathepsin B and release potent toxin monomethyl auristatin E (M). The drug delivery can be monitored by MRI, which is the most common imaging modality for GBM. Our study evaluated if new cathepsin B cleavable nanoparticle accumulate in GBM and cause tumor cell death.

Methods: We synthesized nanoparticles composed of three elements: (1) a ferumoxytol (F) based nanoparticle carrier; (2&3) a cathepsin-responsive valine-citrulline linker (C) and anticancer drug M (FCM), using ferumoxytol chemistry protocol. We hypothesized that intratumoral cathepsin B can cleave on our nanoparticles and release M to kill GBM cells (Figure 1A). The F core enabled in vivo drug tracking with MRI. **In vitro TNP internalization:** U87 GBM cells were incubated with 4nM FCM or F for 72 hours. The iron content in the cells was evaluated with Prussian blue staining and microscopy. **In vivo MRI:** Experiments were approved by the animal care and use committee at Stanford University. 6-8 weeks-old nude mice were stereotactically implanted with U87-GFP/luciferase GBM cells. When tumors reached ~10⁸ photons/seconds in bioluminescence signal, the animals were treated with two intravenous dose of FCM (25 mg/Kg of Fe; 3 mg/Kg of M per dose) on day 1 and 4 or control. Images were acquired on a 11.7T Bruker MRI on day 5 after 1st injection. Pulse sequences included T₂-weighted fast spin echo (FSE, TE = 54 ms, TR = 3500 ms, flip angle = 180° field of view (FOV)= 30×30 mm) and multi-slice multi-echo sequences (MSME, TE = 7.4-59.5 ms, TR = 3000 ms, flip angle = 180°, FOV = 30×30 mm). Tumor area and T₂ relaxation time of the tumor tissues were compared between FCM and control groups using unpaired t test.

Results: We successfully synthesized FCM with hydrodynamic size = 101±8 nm and zeta potential = 5±3 mV, while unconjugated F has a hydrodynamic size = 31±1 nm and zeta potential = -17±5mV. When incubating FCM and F with U87 cells, FCM-treated cells demonstrated significantly higher iron content (98±1% of cells are iron-positive) than F-treated cells (3±1% of cells are iron-positive), as shown in Figure 1B. After several washes to remove the dead and detached GBM cells, we found that alive attached cells were significantly lower in FCM-treated group (3.8±2.0 px²) compared with F-treated group (80.0±14.5 px², p<0001). Preliminary *in vivo* MRI studies demonstrated a tumor signal decline at five days after injection of FCM (T₂ relaxation time 57.9±11.1 ms) but not PBS-injected controls (80.3±2.6 ms) (Figure 1C). On day 5 after intravenous injection, FCM-treated tumors demonstrated a significantly smaller tumor sectional area (2153.0±1400.1 px²) compared to PBS-treated control mice (7322.5±1601.6 px²; Figure 1C).

Discussion: Our data show that new cathepsin B cleavable FCM accumulated in GBM and caused tumor cell death. Ana et al described that larger F yielded enhanced nanoparticle internalization in cells. Coated F with 5 or 20 kDa of polyethylene glycol increased size from 60 nm (uncoated F) to 115 nm (coated F with 5 kDa) and 109 nm (coated F with 20 kDa) respectively. MDA-MB-231 breast human adenocarcinoma and PANC-1 pancreatic human adenocarcinoma barely uptake uncoated F but uptake high amount of coated F. Since coated and uncoated F had similar zeta potential at ~-20mV, the improved uptake is likely due to increased size of coated F. Because cathepsin B is mainly located in lysosomes in cells, FCM have to enter GBM cells to be cleaved by cathepsin B and release drugs.² Our data showed GBM cells uptake more FCM compared to F that was consistent with FCM had larger size. Antibody-drug conjugates studies used antibodies to deliver linked M. Polatuzumab® and Adcetrix® are composed of a cathepsin B cleavable M and a CD79 or CD30 antibody respectively.³ Although they showed some improvements in lymphoma, there are limited data in GBM. EGFR antibody-drug conjugates with non-cleavable linker used in GBM demonstrated ineffective results that may result from incapability of antibodies to cross blood-brain barrier (BBB). Furthermore, antibody-drug conjugates lack of imaging ability and therefore raising the challenges to monitor drug delivery in GBM treatment.⁴ In the animal studies, our intravenously injected FCM was able to cross BBB and accumulate at the tumor. Our developed FCM can enter and kill GBM tumor cells and be imaged by MRI.

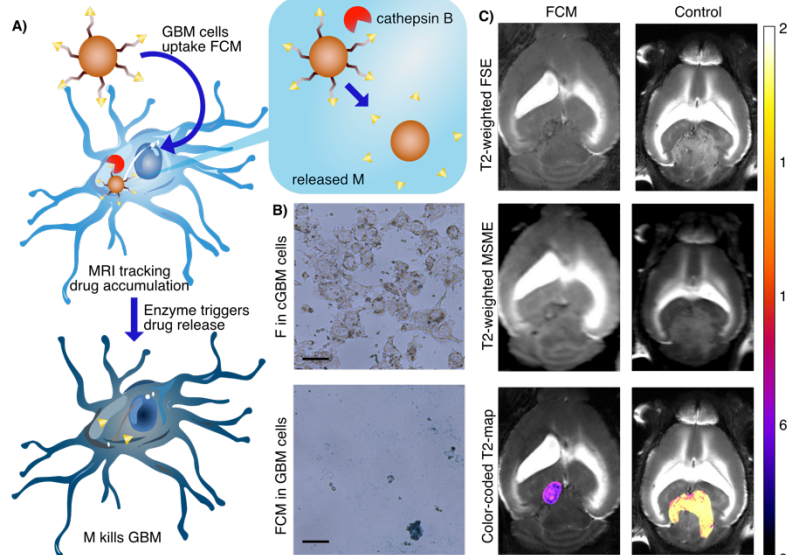


Figure 1. A) GBM cells endocytose FCM. Cathepsin B cleaves FCM to release drug M. B) Representative images of U87 cells treated with FCM or F and stained by Prussian Blue. Upper panel is FH treated U87 cell; lower panel is FCM treated cells. Blue cells indicate iron positive. Scale bar = 200μm. C) Representative coronal T₂-weighted MR images of FCM- and PBS-injected (control) orthotopic GBM mouse brain. Top panel shows FSE image, middle panel shows MSME images, and bottom panel shows color coded T₂ map.

Conclusion: Intravenously injected FCM accumulate in GBM and cause significant tumor death. The nanoparticle carrier in FCM offers *in vivo* drug tracking with MRI.

References: 1)Koh *et al.* Expression of cathepsins B, D, and G in isocitrate dehydrogenase-wildtype glioblastoma. *Front Surg*(2017). 2)Rempel *et al.* Cathepsin B expression and localization in glioma progression and invasion1. *Can Res*(1994). 3)Parakh *et al.* Antibody drug conjugates in glioblastoma – is there a future for them? *Front. Oncol.* (2021). 4)Gan *et al.* Antibody-drug conjugates in glioblastoma therapy: the right drugs to the right cells. *Nat Rev Clin Oncol* (2017).

Acknowledgment: This work was supported by a grant from the national institute for child health and human development (NICHD), grant number R01HD103638.

Fe(III) TACN-based Macrocycles with Various Pendant Donor Groups as MRI probes

Elizabeth A. Kras, Rebecca P. Tarbox, Janet R. Morrow

Department of Chemistry, University at Buffalo, State University of New York

Introduction: While Gd(III) complexes have traditionally been used for paramagnetic MRI contrast agents, high spin Mn(II) and Fe(III) complexes offer alternative options for use as MRI probes.¹ Electronic relaxation times (T_{1e}), water exchange residence times (τ_m), and second sphere water interactions are a few parameters that affect the proton relaxivity by a paramagnetic complex. These parameters have been studied more extensively in Gd(III) and Mn(II) complexes compared to Fe(III) complexes, where additional studies are needed.^{2, 3} Our lab has previously published on Fe(III) TACN-based macrocycles for use as T_1 MRI contrast agents that showed promising relaxivity ($2.2 \text{ mM}^{-1}\text{s}^{-1}$ at 4.7 T, 37 °C), however certain derivatives showed slow clearance through the renal pathway in mice.⁴ The next phase of this research, which will be presented here, involves examining different types of coordinating pendants for Fe(III) complexes and their effect on phantom relaxivity, magnetic field and pH dependence of relaxivity, as well as solubility, and other solution characteristics. Complexes presented here have either three of the same pendants on TACN, or two different coordinating pendant types on TACN.

Methods: Ligands were synthesized using a variety of methods. FeNOHP and FeNOTP were synthesized as reported.⁵ Ligands that contained two hydroxypropyl pendants were synthesized using a modified procedure and the final pendant was added to this precursor by alkylation reactions, reductive aminations, or by Mannich-like reactions.⁴ Ligands were characterized using mass spectrometry and ^1H , ^{13}C , ^{31}P NMR spectroscopy. Metalation of the macrocyclic ligands was done using FeBr_2 or FeCl_3 . Complexes were characterized using ^1H NMR, elemental analysis, and magnetic susceptibility measurements. Phantom T_1 measurements were performed at 1.4 T (60 MHz NMR) and 9.4 T (400 MHz NMR) at 33 °C and 37 °C respectively and samples contained 100 mM NaCl and 20 mM HEPES buffer. T_1 measurements in the presence of HSA contained 35 mg/mL of HSA.

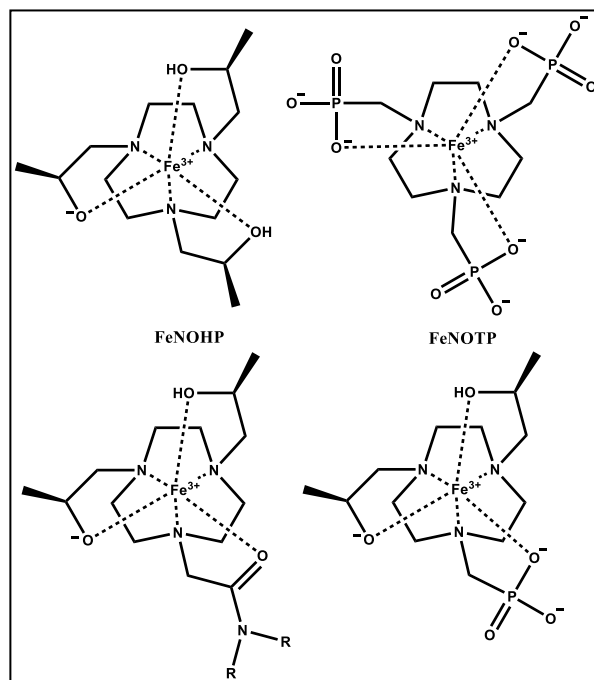
Results: Mass spectrometry and NMR supported the formation of the Fe(III) high spin complex, even when an iron (II) salt was used for metalation. Studies with FeNOTP and FeNOHP show that both have kinetic inertness under biological conditions. FeNOTP showed inertness to dissociation even in concentrated (1 M) acid solutions. Both complexes have electrode potentials around -330 mV, suggesting that the complexes are stabilized as Fe(III) under biologically relevant conditions. Over a range of field strengths (1.4 to 9.4 T), FeNOHP showed higher relaxivity values than FeNOTP. However, FeNOHP showed lower solubility than FeNOTP, at 5 mM and 40 mM respectively. Imaging in mice, determined that FeNOTP had more rapid renal clearance than previously reported compounds from our lab. Intravenous injection of 200 $\mu\text{mol}/\text{kg}$ FeNOTP showed similar blood and kidney pharmacokinetic profiles to injections of 50 $\mu\text{mol}/\text{kg}$ Gd-DOTA. Complexes that contained two hydroxypropyl groups with a different third coordinating pendant typically showed increased solubility when compared to FeNOHP as well as relaxivity values that were lower than their symmetrical counterparts at 1.4 T.

Discussion: High aqueous solubility is an important factor when designing new complexes to be injected *in vivo*, and FeNOTP shows promise, being one of the most soluble Fe(III) macrocyclic complexes our lab has synthesized thus far. However, FeNOTP shows lower relaxivity in comparison to FeNOHP, which is why further studies were performed on complexes with two hydroxypropyl pendants. By changing the third hydroxypropyl pendant from FeNOHP to another coordinating pendant, improvement in the solubility was made. However, in some cases, this increase in solubility came at the detriment of the complexes relaxivity. Alternative pendant groups such as amides also decrease the relaxivity compared to the symmetrical complexes.

Conclusion: Fe(III) high spin complexes were successfully prepared with several TACN-based ligands. Departure from a symmetrical complex with three of the same pendants, such as FeNOHP, to a complex with mixed pendants, resulted in a decrease of relaxivity at 1.4 T; however, for certain pendants such as the phosphonate group, there was an increase in solubility. Studies are underway to better understand the relaxivity differences between the complexes by examination of the magnetic field dependence of relaxivity and studies of the geometry and rigidity of the complexes. Modifications of the ligands reported here, including addition of sites for conjugation or binding to a proteins or peptides, is expected improve the relaxivity of the Fe(III) complexes.

References:

- Lauffer, R. B., Paramagnetic metal complexes as water proton relaxation agents for NMR imaging: theory and design. *Chem. Rev.* **1987**, 87 (5), 901-927.
- Wahsner, J.; Gale, E. M.; Rodríguez-Rodríguez, A.; Caravan, P., Chemistry of MRI Contrast Agents: Current Challenges and New Frontiers. *Chem. Rev.* **2019**, 119 (2), 957-1057.
- Botta, M.; Carniato, F.; Esteban-Gómez, D.; Platas-Iglesias, C.; Tei, L., Mn(II) compounds as an alternative to Gd-based MRI probes. *Future Med. Chem.* **2019**, 11 (12), 1461-1483.
- Snyder, E. M.; Asik, D.; Abozeid, S. M.; Burgio, A.; Bateman, G.; Turowski, S. G.; Spernyak, J. A.; Morrow, J. R., A Class of FeIII Macrocyclic Complexes with Alcohol Donor Groups as Effective T_1 MRI Contrast Agents. *Angew. Chem. Int. Ed.* **2020**, 59 (6), 2414-2419.
- Kras, E. A.; Abozeid, S. M.; Eduardo, W.; Spernyak, J. A.; Morrow, J. R., Comparison of phosphonate, hydroxypropyl and carboxylate pendants in Fe(III) macrocyclic complexes as MRI contrast agents. *J.Inorg. Biochem.* **2021**, 225, 111594.



Feasibility and Challenges of *In Vivo* Hyperpolarized Imaging of MR Biosensors with Ultra-Low Gamma Nuclei

Qing Wang,¹ Jun Chen,² Wirya Feizi,¹ Asiyeh Asaadzade,¹ Zoltan Kovacs,² Jae Mo Park,² and Lloyd Lumata^{1,3}

¹Department of Physics, University of Texas at Dallas, Richardson, TX. ²Advanced Imaging Research Center, University of Texas Southwestern Medical Center, Dallas, TX. ³Department of Neuroscience, University of Texas at Dallas, Richardson, TX.

Introduction. Dissolution dynamic nuclear polarization (DNP) is a versatile hyperpolarization technique that endows high liquid-state nuclear magnetic resonance (NMR) sensitivity to a variety of nuclei that have relatively long spin-lattice relaxation time T1 at physiologically-tolerable temperature. Among the nuclei, ¹³C (gamma = 10.7 MHz/T) is the foremost target for hyperpolarization due to its utility in metabolic and biochemical imaging as seen in a plethora of hyperpolarized ¹³C MR studies using ¹³C-pyruvate and other ¹³C-labeled metabolic tracers. Although less sensitive than ¹³C, ¹⁵N-labeled (gamma = 4.31 MHz/T) biosensors have also been reported in a select number of hyperpolarized (HP) MR studies. In this presentation, ultra-low gamma nuclei are defined as nuclei with gyromagnetic ratios that are lower than that of ¹⁵N nucleus. Herein, we report on the feasibility of and the challenges involved in using biosensors with ultra-low gamma in *in vivo* hyperpolarized MR imaging, specifically with the use of ⁸⁹Y (gamma = 2.086 MHz/T) biosensors *in vivo*. ⁸⁹Y is a very attractive nucleus for the design of responsive MR probes (e.g. pH-sensing capability using HP ⁸⁹Y-EDTMP shown in Fig. 1)¹ because of the sensitivity of the ⁸⁹Y NMR chemical shift to changes in the coordination environment of the Y³⁺ ion and the relatively long T1 reported up to 600 s.² The hyperpolarized ⁸⁹Y data set herein will be discussed in light of current instrumental capability and limitations as well as its implications on potentially using other ultra-low gamma nuclei in HP imaging such as ¹⁰⁶Ag, ¹⁰⁹Ag, and other nuclei.

Methods. Y-DOTA and Y-EDTMP complexes were synthesized as described previously.^{1,2} 0.5 M of ⁸⁹Y-complex was prepared in a solution containing 75% water and 25 % glycerol by volume and doped with 15 mM trityl OX063 free radical plus 2 mM Gd-HP-DO3A complex (ProHance). 100 uL aliquots of these DNP samples were inserted into either the 3.35 T commercial Hypersense DNP polarizer (Oxford Instruments Biotools, UK) or the 4.6 T homebuilt dissolution hyperpolarizer at UT Southwestern Medical Center. For *in vivo* studies, the HP-⁸⁹Y-DOTA solution was administered to healthy male Fischer rats (~200 g) by intravenous injection through the tail vein as a bolus (0.125 mmol/kg body weight, up to 4.0 mL, injection rate = 0.25 mL/s), immediately followed by a dynamic ⁸⁹Y MRS scan (pulse-and-acquire with 90° hard pulse RF excitation and repetition time = 10 sec). Hyperpolarized ⁸⁹Y MR detection was done using homebuilt 1H and ⁸⁹Y RF surface coils tuned to a 3 T Varian VNMRS small animal MRI scanner.

Results and Discussion. Yttrium complexes are interesting due to the similarity of their chemistry with gadolinium complexes that are used as MR contrast agents such as pH, zinc levels, and other extracellular biological milieu. An example is displayed in Fig. 1 in which hyperpolarized ⁸⁹Y-EDTMP complex can be used for physiological pH detection.¹ The potential pH sensing capability of HP ⁸⁹Y-EDTMP emanates from the NMR sensitivity of ³¹P to the protonation of the non-coordinating phosphonate oxygens, which in turn is indirectly detected by ⁸⁹Y in the complex in the form of chemical shift change. Fig. 2 demonstrates the feasibility of detecting HP ⁸⁹Y NMR signal *in vivo* as detected in the abdominal rea of the rat after bolus injection of HP ⁸⁹Y-DOTA. Although *in vivo* HP ⁸⁹Y detection is feasible with 60,000-fold liquid-state ⁸⁹Y NMR enhancement of HP ⁸⁹Y-DOTA (when measured at 9.4 T and 37 deg C), this enhancement corresponds to only 10% ⁸⁹Y DNP-enhanced polarization.² Thus, there is still a substantial room for improvement in terms of sensitivity enhancement that needs to be addressed to improve the resolution of HP MR imaging using ⁸⁹Y biosensors *in vivo*. Instrumental improvements such as DNP at higher magnetic fields (e.g. 7 T), lower temperature, and the potential use of cross-polarization and microwave frequency modulation are suggested and underway in pursuit of higher ⁸⁹Y DNP-enhanced polarization for *in vivo* HP ⁸⁹Y MR applications.

Conclusion. *In vivo* detection of hyperpolarized ⁸⁹Y MR signal is feasible as demonstrated. This potentially opens the door to the use of other chemical shift-based, yttrium complex analogs of Gd-based MR biosensors for pH, Zn, and other extracellular biological milieu. The highest recorded DNP-enhanced ⁸⁹Y polarization is so far only 10%. Further increase in current ⁸⁹Y DNP enhancements is needed to improve the utility and resolution of HP ⁸⁹Y-based MR biosensors as well as other ultra-low gamma nuclei in *in vivo* applications.

- References:** (1) Wang Q, Niedbalski P, Parish C, Ratnakar J, Kovacs Z, Lumata L, Hyperpolarized ⁸⁹Y-EDTMP as chemical shift-based NMR sensor for pH at the physiological range, *J. Magn. Reson.* 320, 106837(2020).
 (2) Lumata L, Jindal AK, Merritt ME, Malloy CR, Sherry AD, Kovacs Z. DNP by thermal mixing under optimized conditions yields >60,000-fold enhancement of ⁸⁹Y NMR signal. *J Am Chem Soc.* 133, 8673-8680 (2011).

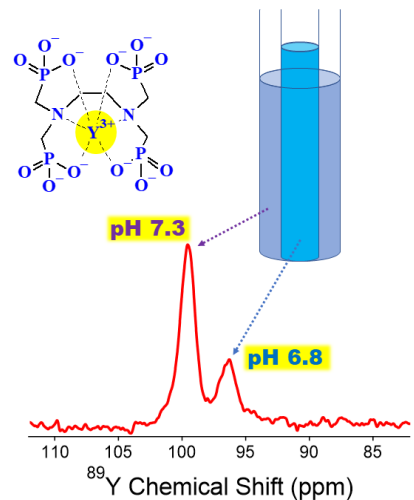


Fig. 1. pH detection using hyperpolarized ⁸⁹Y-EDTMP complex.

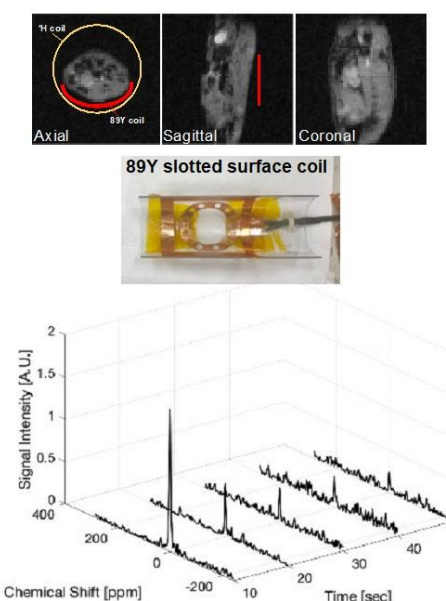


Fig. 2. *In vivo* hyperpolarized ⁸⁹Y MR detection in rat abdominal area.

10%. Further increase in current ⁸⁹Y DNP enhancements is needed to improve the utility and resolution of HP ⁸⁹Y-based MR biosensors as well as other ultra-low gamma nuclei in *in vivo* applications.

- References:** (1) Wang Q, Niedbalski P, Parish C, Ratnakar J, Kovacs Z, Lumata L, Hyperpolarized ⁸⁹Y-EDTMP as chemical shift-based NMR sensor for pH at the physiological range, *J. Magn. Reson.* 320, 106837(2020).
 (2) Lumata L, Jindal AK, Merritt ME, Malloy CR, Sherry AD, Kovacs Z. DNP by thermal mixing under optimized conditions yields >60,000-fold enhancement of ⁸⁹Y NMR signal. *J Am Chem Soc.* 133, 8673-8680 (2011).

Computationally designed multicolored-MRI reporter genes

Hyla Allouche-Arnon, Olga Khersonsky, Sarel J. Fleishman, Amnon Bar-Shir

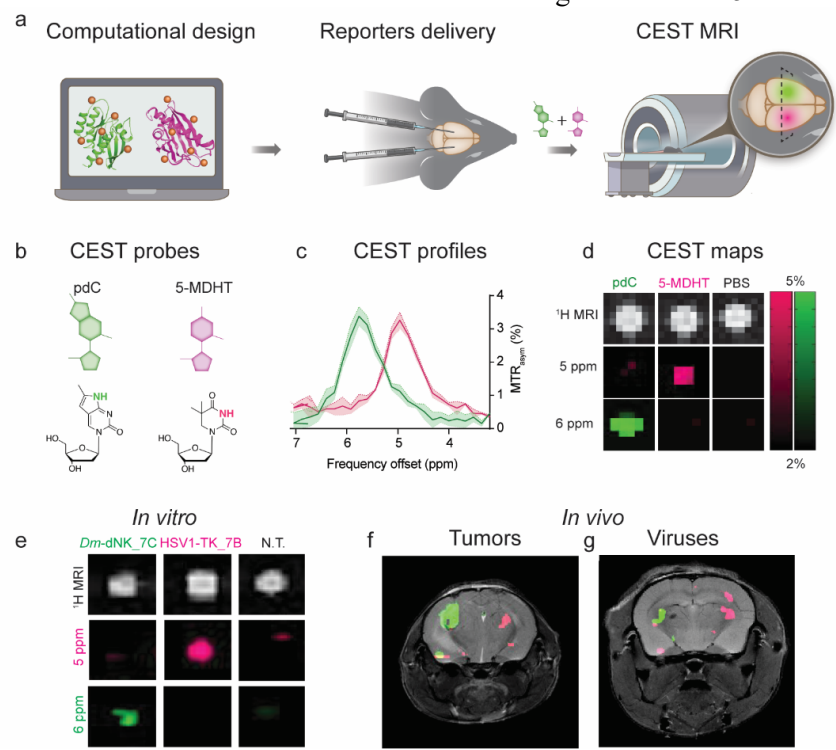
Weizmann Institute of Science, Rehovot, 7610001, Israel

Introduction: Recent advances in tissue clarification¹ enabled 3D multiplexed mapping of genetically engineered reporters in excised organs postmortem. Yet this approach is not applicable to noninvasive *in vivo* studies of dynamic and complex cellular events. Reporter genes developed for MRI present an alternative solution for *in vivo* mapping of transgene expression. However, MRI reporter genes are limited in possessing the multiplex imaging capabilities needed for the simultaneous “illumination” of cellular processes. Moreover, a major pitfall for advanced developments of MRI reporter genes is the low-throughput capabilities of MRI-guided screening preclude the large-scale mutagenesis campaigns that have served so well in engineering fluorescent proteins.² Here, we capitalized on the frequency encodability CEST MRI to obtain MRI-based colors,³ combined with an automated and computational evolution-based protein design method (PROSS)⁴ to design fully orthogonal genetically engineered MRI reporter genes (Fig. 1a).⁵

Methods: *Computational model for dNK mutations:* The PROSS algorithm was applied on *Dm*-DNK and HSV1-TK using the online webserver (<http://pross.weizmann.ac.il>), resulting in final variants, HSV1-TK_7B or *Dm*-dNK_7C, showing high expression and improved enzymatic activity. *CEST MRI: In vitro and in vivo* CEST MRI experiments were carried out on a 15.2T scanner, using a RARE sequence (TR/TE = 6000/20 ms, RARE factor 8), including a CEST module with a $B_1 = 3.6 \mu\text{T} / 4 \text{ sec}$, $\pm 10 \text{ ppm}$. *Inoculation of tumors and viruses:* Stable CHO^{HSV1-TK_7B} and CHO^{*Dm*-dNK_7C} cell lines or AAV^{*Dm*-dNK_7C} and AAV^{HSV1-TK_7B} viral constructs were intracranially injected into the striatum of 8-wks-old mice to generate intracranial tumors or viral infection respectively, in both hemispheres. Seven (CHO cells) or 14 (AAV solutions) days post inoculation mice were anesthetized and examined with MRI before and after an injection of a mixture of 5-MDHT and pdC (Fig. 1b).

Results and discussion: First, we evaluated the CEST-MRI pseudo-color encoding of 5-MDHT and pdC. The MTR_{asym} plots (Fig. 1c) showed negligible signal overlaps at $\Delta\omega$ s of 5ppm (for 5-MDHT) and 6ppm (for pdC) enabling their mapping using pseudo-MRI-colors (Fig. 1d). We then used the PROSS protein-stability design algorithm followed by a single point mutagenesis to obtain orthogonal dNK/substrate pairs, namely HSV1-TK_7B/5-MDHT and *Dm*-dNK_7C/pdC. Then CHO^{HSV1-TK_7B} and CHO^{*Dm*-dNK_7C} cells were incubated with 5-MDHT and pdC mixture solution followed by examination of their CEST-MRI characteristics to show a clear, well-separated dual-colored CEST maps (Fig. 1e). Finally, we evaluated the *in vivo* performance of the developed approach. For all studied animals two CEST-MRI datasets were acquired, before and after intravenous administration of a solution containing a mixture of 5-MDHT and pdC. Subtracting the MTR_{asym} maps ($\Delta\omega$ s of 5 and 6 ppm) obtained after the injection of the probes mixture from those obtained prior the injection resulted in a pseudo-colored CEST map. In both studied animal models (7 days after intracranial injection of CHO^{*Dm*-dNK_7C} and CHO^{HSV1-TK} cells, Fig. 1f; or 14 days after the delivery of AAV^{*Dm*-dNK_7C} and AAV^{HSV1-TK_7B}, Fig. 1g) clear pseudo-colored CEST maps were obtained.

Conclusion: We demonstrated here the development and implementation of a genetically encoded reporter system, which enables MRI mapping transgene expression in a pseudo-multi-color fashion. Our approach extends the “multicolor” toolbox to thus far inaccessible deep tissues in live subjects. Our work demonstrates that new protein-design methods can be applied to systems that are recalcitrant to conventional high-throughput screening in order to generate highly desirable properties.



References: 1. Chung, K. et al. *Nature* **2013**, 497 (7449), 332-7. 2. Shaner, N. C. et al. *Nat Biotechnol* **2004**, 22 (12), 1567-72. 3. McMahon, M. T. et al. *Magn Reson Med* **2008**, 60 (4), 803-12. 4. Goldenzweig, A. et al. *Mol Cell* **2016**, 63 (2), 337-346. 5. Allouche-Arnon, H. et al. *Nat Biotechnol* **2022** Accepted. <https://doi.org/10.5281/zenodo.5594956>.

Imaging molecular functions in the brain with MR contrast agents

E.L. Bearer, T.W. Uselman, H.B. Gray, and R.E. Jacobs

University of New Mexico Health Sciences Center, Albuquerque, NM; Beckman Institute, California Institute of Technology, Pasadena, CA, and Zilkha Neurogenetic Institute, University of Southern California, Los Angeles, CA

Manganese-enhanced magnetic resonance imaging (MEMRI), for T_1 contrast, and intravascular ultrasmall superparamagnetic particles (USPIO) for T_2 , holds exceptional promise for preclinical studies of brain-wide physiology³. Physiological contrast agents report on how perturbation of specific molecules, altered either genetically or pharmacologically, effect function such as axonal transport, neural activity or cerebral blood flow (CBF).

Longitudinal MEMRI offers a powerful platform to witness functional effects of molecular perturbations, such as gene knockouts in mice. Mn(II) is powerful for two main reasons: 1) Strong effect at low doses; 2) Sensitive to biological interactions, such as projection tracing and neural activity mapping via entry into electrically active neurons in the living brain. High-spin Mn(II) reduces the relaxation time of nearby water protons: at Mn(II) concentrations typically encountered in MEMRI, robust hyperintensity is obtained without adverse effects. When delivered by stereotactic intracerebral injection, Mn(II) enters active neurons at the injection site and then travels inside axons for long distances, tracing neuronal projection anatomy. When delivered systemically, Mn(II) enters active neurons throughout the brain via voltage-sensitive calcium channels and clears slowly. Thus behavior can be monitored during Mn(II) uptake and hyperintense signals due to Mn(II) accumulation captured retrospectively, allowing pairing of behavior with neural activity maps for the first time⁴. Because of its independence from vascular dynamics, MEMRI may be the only method to witness effects of molecules, like cocaine, that affect both vascular and neural dynamics. We reported axonal transport dynamics in 8 different genetically altered mice with MEMRI producing clinically useful results^{2,5-12}. USPIO are powerful for similar reasons, giving a strong effect size for measurement of CBF. One of us has reported effects CBF in living mice^{1,13}. Automated computational processing allows data-driven, unbiased comprehensive analysis of image stacks from multiple individuals, yielding statistical significance^{14,15}. The Bruker Biospin 11.7T MR scanner in the Beckman Institute at Caltech, and the newly updated Bruker Biospec/Avance 7T/30 cm and the Bruker BioSpec 7T/30USR at UNM's new Brain and Behavioral Health Institute, provide high resolution 4D images of living mouse brains at 100 μ m isotropic voxels over time for physiological detection of molecular effects.

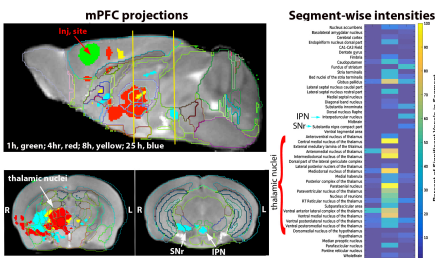


Fig. 1. Example of MEMRI tract tracing in NET deleted mice²

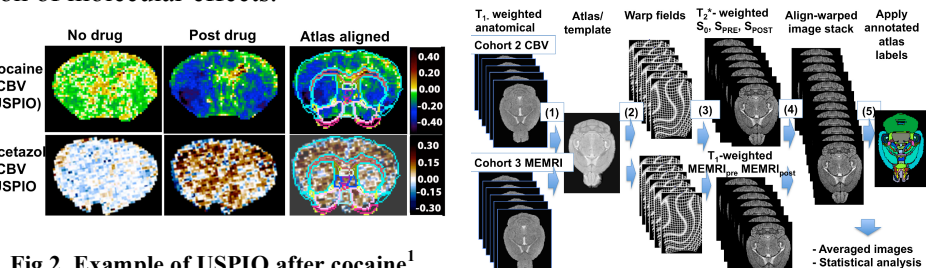


Fig. 2. Example of USPIO after cocaine¹

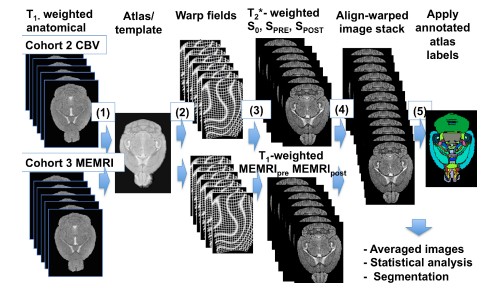


Fig. 3. Bearer Lab computational processing steps.

References:

1. Perles-Barbacaru, T.-A., Procissi, D., Demyanenko, A.V. & Jacobs, R.E. Quantitative pharmacologic MRI in mice. *NMR in Biomedicine* **25**, 498-505 (2012).
2. Gallagher, J.J. et al. Altered reward circuitry in the norepinephrine transporter knockout mouse. *PLoS One* **8**, e57597 (2013).
3. Uselman, T., Medina, C., Gray, H., Jacobs, R. & Bearer, E. Longitudinal manganese-enhanced magnetic resonance imaging of neural projections and activity. *NMR in Biomed* (2022).
4. Uselman, T.W., Barto, D.R., Jacobs, R.E. & Bearer, E.L. Evolution of brain-wide activity in the awake behaving mouse after acute fear by longitudinal manganese-enhanced MRI. *NeuroImage* **222**, 116975 (2020).
5. Bearer, E.L. et al. Role of neuronal activity and kinesin on tract tracing by manganese-enhanced MRI (MEMRI). *Neuroimage* **37 Suppl 1**, S37-46 (2007).
6. Bearer, E.L. et al. Alterations of functional circuitry in aging brain and the impact of mutated APP expression. *Neurobiol Aging* **70**, 276-290 (2018).
7. Bearer, E.L., Zhang, X. & Jacobs, R.E. Live imaging of neuronal connections by magnetic resonance: Robust transport in the hippocampal-septal memory circuit in a mouse model of Down syndrome. *Neuroimage* **37**, 230-42 (2007).
8. Bearer, E.L., Zhang, X., Janvelyan, D., Boulat, B. & Jacobs, R.E. Reward circuitry is perturbed in the absence of the serotonin transporter. *Neuroimage* **46**, 1091-104 (2009).
9. Gallagher, J.J., Zhang, X., Ziomek, G.J., Jacobs, R.E. & Bearer, E.L. Deficits in axonal transport in hippocampal-based circuitry and the visual pathway in APP knock-out animals witnessed by manganese enhanced MRI. *Neuroimage* **60**, 1856-66 (2012).
10. Medina, C.S. et al. Hippocampal to basal forebrain transport of Mn²⁺ is impaired by deletion of KLC1, a subunit of the conventional kinesin microtubule-based motor. *Neuroimage* **145**, 44-57 (2017).
11. Medina, C.S. et al. Decoupling the Effects of the Amyloid Precursor Protein From Amyloid-beta Plaques on Axonal Transport Dynamics in the Living Brain. *Front Cell Neurosci* **13**, 501 (2019).
12. Zhang, X. et al. Altered neurocircuitry in the dopamine transporter knockout mouse brain. *PLoS One* **5**, e11506 (2010).
13. Perles-Barbacaru, T.-A. et al. Quantitative pharmacologic MRI: Mapping the cerebral blood volume response to cocaine in dopamine transporter knockout mice. *NeuroImage* **55**, 622-628 (2011).
14. Delora, A. et al. A simple rapid process for semi-automated brain extraction from magnetic resonance images of the whole mouse head. *J Neurosci Methods* **257**, 185-93 (2016).
15. Medina, C.S., Manifold-Wheeler, B., Gonzales, A. & Bearer, E.L. Automated Computational Processing of 3-D MR Images of Mouse Brain for Phenotyping of Living Animals. *Curr Protoc Mol Biol* **119**, 29A 5 1-29A 5 38 (2017).